Quality Assurance for Mixed Electron-photon Beam Radiation Therapy using Treatment Log files and MapCHECK

Yee Man Tai

Medical Physics Unit, Department of Oncology

McGill University, Montreal

May, 2022

A thesis submitted to McGill University in partial fulfillment of the requirements of the degree of Master of Science in Medical Radiation Physics

Abstract

Mixed electron-photon beam radiation therapy (MBRT) is an emerging treatment technique that combines both particles in a single plan to exploit their advantageous characteristics. An MBRT plan uses multiple beam energies and a large number of apertures to achieve a highly conformal dose to the target volume. However, the complexity of the technique makes it more prone to error. This project aims to develop a comprehensive QA protocol for MBRT, and we explored the possibility of utilizing trajectory log files and MapCHECK, a 2D diode array detector, for MBRT plan verification. In this study, 2 MBRT plans were robustly optimized for 2 soft tissue sarcoma (STS) patients. One of the plans was delivered repeatedly on 3 different linacs to account for the inter-linac and intra-linac differences in deliveries. Treatment log files for 12 deliveries were collected to retrieve axis data for 3D dose reconstruction. Dose calculations were performed with Monte Carlo methods using EGSnrc. The log file-recalculated mean dose to the clinical target volume (CTV) and three organs at risk (OAR) of the patient were computed and compared to the planned dose. The deviations between the recalculated and the planned dose to the CTV were below 0.1 % for all deliveries. The log file-recalculated dose was in excellent agreement with the planned dose with no significant inter and intra-linac dif-

ference. Both MBRT plans were also delivered to the MapCHECK with collapsed gantry angle. A MapCHECK Monte Carlo phantom was modelled for dose simulations in the MapCHECK using EGSnrc. The agreement between the measured and calculated dose distribution was evaluated using gamma analysis with the gamma criteria of 3%/2mm. The gamma passing rate varied between 84.55 % and 97.78 %, depending on the plan and the delivery distance. The agreement between MapCHECK measurement and simulation was excellent for the electron deliveries at an SAD of 80 cm but deteriorated with increased SAD to 100 cm.

Abrégé

La radiothérapie à faisceau mixte (MBRT) est une technique émergente qui combine l'utilisation de faisceau d'électrons et de photons dans un seul plan de traitement afin d'exploiter leurs caractéristiques avantageuses. Un plan MBRT utilise des faisceaux de multiples énergies et un grand nombre d'ouvertures afin d'atteindre une dose hautement conforme au volume cible. Toutefois, dû à sa complexité, la technique de MBRT est plus propice à l'erreur. Ce projet vise à développer un protocole complet d'assurance qualité pour MBRT. Nous avons exploré la possibilité d'utiliser les fichiers journaux de trajectoire et un détecteur à barrettes de diodes MapCHECK pour la vérification de plans MBRT. Dans cette étude, deux plans MBRT ont été robustement optimisés pour deux patients atteints d'un sarcome des tissus mous. Un des plans a été administré à plusieurs reprises sur trois linacs différents pour tenir compte des différences inter-linac et intra-linac. Les fichiers journaux de la trajectoire ont été collectés pour 12 administrations. Les données d'axes provenant de fichiers journaux sont utilisées pour des reconstructions 3D de la dose. Ces calculs sont effectués par méthode Monte Carlo avec le moteur de calcul EGSnrc. La dose moyenne au volume-cible clinique (CTV) et à 3 organes à risque du patient ont été reconstituées à partir des fichiers journaux et comparées à la dose planifiée. La variation

entre la dose reconstituée et la dose planifiée au CTV était inférieure à 0.1 % pour toutes les administrations. La dose reconstituée était en excellente accord avec la dose planifiée sans aucune significante différence inter- ni intra-linac. Les deux plans MBRT ont été administrés au MapCHECK avec l'angle du portique fixé verticalement. Un fantôme Monte Carlo de MapCHECK a été modelé pour des simulations de dose dans le MapCHECK avec EGSnrc. L'accord entre la distribution de la dose mesurée et la dose calculée ont été évaluée par analyse gamma avec un critère gamma de 3 %/2 mm. Les taux de passage ont varié entre 84.55 % et 97.78 %, dépendamment du plan et de la distance de l'administration. L'accord entre les mesures MapCHECK et la simulation était excellent pour l'administration d'électrons à une distance à la source (SAD) de 80 cm mais s'est détérioré lorsque la SAD a été augmentée à 100 cm.

Acknowledgements

First and foremost, I would like to express my deepest gratitude to my supervisor, Professor Jan Seuntjens, for giving me the opportunity to participate in this project. This study would not be possible without his expertise, guidance and patience. He has always been very caring and supportive, and has provided me with great advice in both my study and future career.

I would like to thank Dr. Monica Serban, Dr. Tanner Connell and Michael Evans for their guidance on the use of dosimetry instruments and their advice in measurement setups throughout this study. I am so thankful for having the opportunity to perform experiments in the clinic and gain hands-on experience in using radiotherapy equipment.

I would also like to thank Marc-André Renaud for his fundamental work in mixed-beam radiation therapy and the development of the in-house web-based treatment planning system, Brems. His work has been a cornerstone for this project.

Very importantly, I would like to express my sincere thanks to Veng Jean Heng for being my mentor and my dearest friend throughout the year. I cannot thank him enough for his enormous support both inside and outside the academic setting.

I would like to acknowledge the financial support for this work provided by the Canadian Institutes of Health Research.

I would like to thank all the faculty and staff in the Medical Physics Unit for their patience in teaching. My thanks also go to Margery Knewstubb and Tatjana Nisic for handling all the administrative work.

I would also like to thank all my friends and classmates in the MPU for their kindness and support. They have made my studies more enjoyable.

Finally, I would like to thank my family and my boyfriend who have always been giving me love and encouragement unconditionally.

Table of Contents

List of Figures

List of Tables

Chapter 1

Background and Introduction

This chapter discusses briefly the development of radiation therapy from the first therapeutic use of radiation to modern radiotherapy techniques. It covers the procedures and methods for quality assurance in external beam radiotherapy. The motivation and objective of this thesis will also be given at the end of the chapter.

1.1 Radiation Therapy

Radiation therapy is a type of cancer treatment that uses high-energy particles to kill tumour cells. The high-energy radiation beams are generated and delivered by a linear accelerator, or a linac. In this section, we will review the progress in radiotherapy and the design of a medical linac. We will also briefly go through some modern treatment modalities in external beam radiotherapy.

1.1.1 History of Radiation Therapy

The beginning of radiation therapy was marked by the discovery of X-rays by a German physicist, Wilhelm Conrad Roentgen, in 1895 [29]. The penetrability of X-rays was evidenced by the photographic plate showing Roentgen's wife Bertha's hand. The first therapeutic use of X-rays happened a year after. Émil Herman Grubbé, an American doctor, attempted to treat her breast cancer patient by exposing her lesion with X-rays for about one hour in a single treatment [26, 40].

In the early 1950s, the first medical linac was installed at Hammersmith Hospital, London. It was capable of producing an 8 MV X-ray beam and was put into practice in 1953 [23]. In the next decade, many more clinical linacs were manufactured and became operational around the world. However, the performance of most early machines was limited by low beam energy and radiation output due to the immature waveguide design and power source [65]. The fully stable isocentric linacs capable of producing multiple choice of energies became gradually available in the 1970s. Since then, the linac has become the most commonly used medical device in radiation therapy.

Nowadays, medical linacs have further evolved into more sophisticated systems that are versatile, user-friendly and safe to use. Most of them are well-equipped with imaging systems for dose verification or target tracking. The implementation of the multileaf collimator (MLC) also paves the way for radiation beam shaping and modulation to achieve exceptional dose distributions. The components of modern medical linacs will be discussed in more detail in the following sections.

1.1.2 Cancer and Radiotherapy

Cancer has been one of the deadliest diseases in human history. According to the International Agency for Research on Cancer (IARC), the disease is causing approximately 10 million deaths every year globally. Cancer is a type of tumour that is characterized by uncontrolled cell growth and the ability to metastasize. Radiotherapy utilizes high-energy radiation beam to kill cancer cells [10]. A radiation beam can be composed of charged particles such as electrons or protons or uncharged particles like photons or neutrons. The beam deposits energy to cancer cells through either direct or indirect ionization, which, in turn, induces damage to their genetic material, DNA. The molecular structure of DNA is disrupted either directly by the energy deposited by the radiation beam or through the interactions with highly reactive free radicals. When the cancer cells fail to repair the damage to their DNA, they stop dividing and eventually die.

1.1.3 Linac Design

Medical linacs are machines that accelerate charged particles to generate a high-energy radiation beam that is aimed toward the region of tumour cells in the patient's body. The formation of the radiation beam is carried out by six classes of operating components, namely the injection system, RF power generation system, accelerating waveguide, auxiliary system, beam transporting system, and the beam collimation and beam monitoring system [23]. The main components of a medical linac are shown in Fig. 1.1.

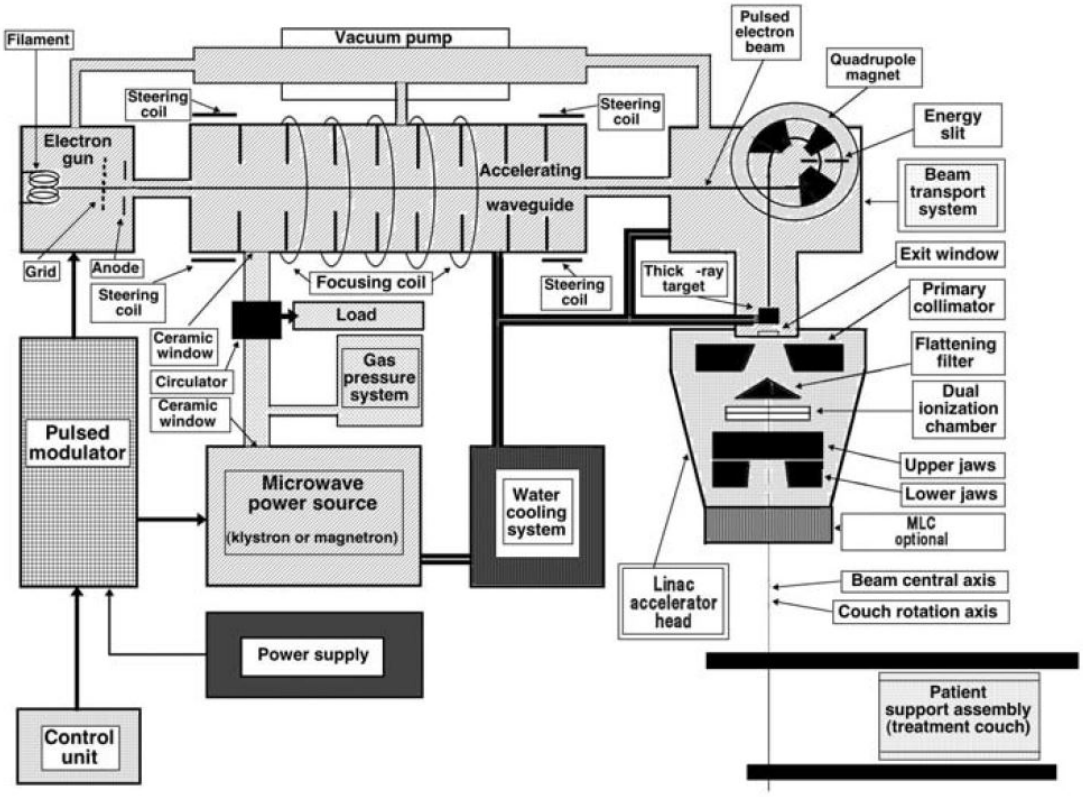

Figure 1.1: The schematic diagram of a medical linac [55].

Beam generation

The injection system is an electron gun that injects electrons into the accelerating waveguide through thermionic emission. The RF power generating system consists of an RF power source and a pulsed modulator which provides high voltage, high current, and short-duration pulses for the RF power source and the electron gun. Waveguides are metallic structures that propagate electromagnetic waves in a preferred direction. The generated RF power is transported by the power transmission waveguide to the accelerating waveguide, which transfers energy from the high power RF fields to the electrons and accelerates them to the desired kinetic energy. The auxiliary system is not directly responsible for electron acceleration, but it maintains the normal functioning of the linac. It

includes a vacuum pumping system, a water cooling system, an air pressure system and shielding to prevent radiation leakage. The electrons exit from the accelerating waveguide will enter the beam transporting system in which they are directed by bending magnets to either the beam exit window or the X-ray target.

Beam delivery

Before being delivered to the patient, the pencil beam is modified into a clinically useful form by the beam collimation and beam monitoring system in the linac treatment head. To deliver photon beams, the accelerated electrons first strike the X-ray target to produce bremsstrahlung photons. Then, a flattening filter is used to flatten the intensity of the photon beam. The primary collimator, secondary collimator, and multileaf collimator (MLC) are collimation devices that determine the shape and size of the photon radiation field according to the tumour region. For electron beam delivery, the target and the flattening filter in the beam path are replaced with a scattering foil which scatters the electron pencil beam over a larger area. Finally, the dose monitoring systems are ionization chambers that monitor the output and the quality of the beam during the delivery to ensure safety and accuracy.

1.1.4 Treatment Planning in External Beam Radiotherapy

A radiotherapy treatment is planned based on the information concerning the target volume in the patient's body. The 3D structure of the target and the surrounding organs at risk (OARs) can be obtained through different imaging modalities, including computed tomography (CT) and Magnetic resonance imaging (MRI). Upon acquiring the anatomi-

cal information of the patient, the target volume and the OARs will be delineated on CT slices by the clinicians. The procedure is known as contouring [54]. Once the target is outlined, some critical structure volumes are defined for treatment planning, namely the gross tumour volume (GTV), clinical target volume (CTV), internal target volume (ITV) and planning target volume (PTV).

The GTV includes only the visible tumour volume on the medical image without adding any margin. The CTV covers the area outside the GTV that may contain microscopic malignant diseases to be cured. It is usually defined to be the 1 cm extension from the GTV. The ITV is drawn by considering the changes in size and position of the CTV due to organ motions. The PTV is often depicted by adding a 0.5 cm margin to the CTV to account for the effect of all possible geometrical variations caused by setup uncertainties and patient motions [31]. The typical geometrical relationship among the four volumes is illustrated in Fig. 1.2.

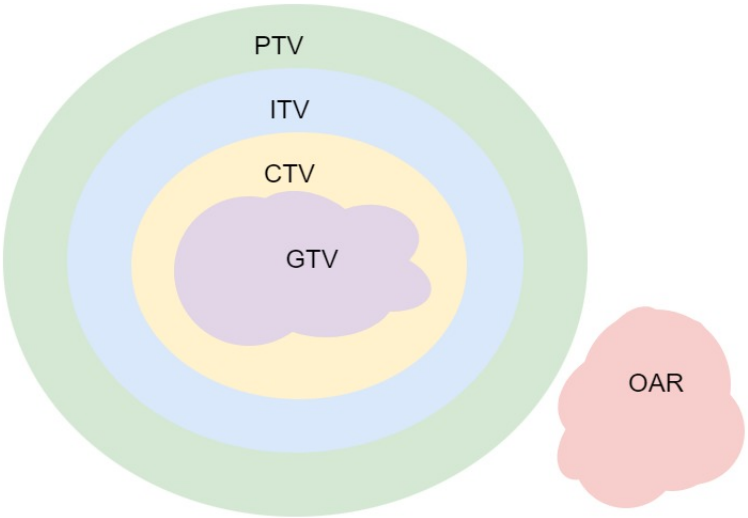

Figure 1.2: The diagram showing the typical relationship among the GTV, CTV, ITV, PTV and an OAR.

1.1.5 Treatment Modalities in External Beam Radiotherapy

There are various treatment modalities in external beam radiotherapy (EBRT). In this section, we will go over some common techniques using photons or/and electrons.

3D Conformal Radiation Therapy (3D-CRT)

3D conformal radiation therapy is a conventional treatment technique which photon beams are shaped according to the 3D structure of the tumour. With the detailed information obtained from the CT images of the patient, physicists decide the direction and shape of the radiation field such that the dose can be accurately delivered to the cancerous cells. The technique is relatively simpler and more efficient, however, radiation to surrounding normal tissues is inevitable.

Intensity Modulated Radiotherapy (IMRT) and Volumetric Modulated Arc Therapy (VMAT)

Intensity-modulated radiotherapy is a modern technique that delivers non-uniform photon beam intensities with the help of computerised inverse planning [62]. In IMRT, each beam is further divided into smaller beamlets with different intensity levels. This enables the delivery of a highly conformal dose to the target region while reducing the dose to healthy tissues. The radiation fields in IMRT are accurately shaped by the MLC, which typically consists of 20 - 80 independent movable leaves arranged in pairs [17] (Fig. 1.3).

In contrast to 3D-CRT, which uses forward planning, IMRT employs inverse planning methods. The desired treatment outcomes, in terms of the prescribed target dose and the

Figure 1.3: A picture showing the 120 Millenium multileaf collimator (Varian Medical Systems, Palo Alto, CA) [16].

maximum OARs dose, are first specified and input into the computer system. Based on the dose objectives and constraints, an objective function is defined as a mathematical description of the treatment plan quality [50]. To optimize the plan, the objective function is minimized by adjusting the beamlet weight. A comparison between the treatment plan for 3D-CRT and IMRT is shown in Fig. 1.4.

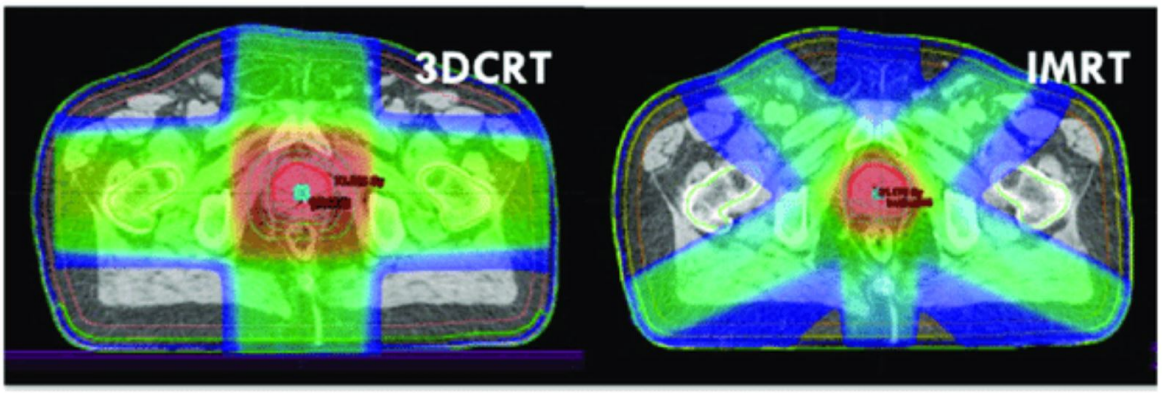

Figure 1.4: The treatment plan for 3D-CRT (left) and for IMRT (right) [60].

In a conventional IMRT treatment, the radiation beam is turned off when the gantry rotates from one delivery angle to the next one. This is known as the "step-and-shoot" delivery. At each gantry angle, the beam is modulated by moving MLC leafs, which is called the dynamic MLC (DMLC). Volumetric modulated arc therapy (VMAT) is an advanced IMRT technique in which the gantry rotates with the beam on during the course of the treatment. During the rotation, the MLC leaves are in constant motion to modulate the beam intensity. This method allows the delivery of radiation in a single arc efficiently, but it requires more complex and time-consuming planning and QA processes [64].

Modulated Electron Radiotherapy (MERT)

Compared to photons, electrons have a shorter practical range that makes them more suitable for treating superficial cancers and sparing deeper healthy tissues. Due to the scattering property of electrons, the penumbra of an electron beam increases significantly with depth [37]. Therefore, electron beam applicators are often positioned at a small distance (a few centimetres) from the patient for electron beam collimation. Conventional electron radiotherapy involved the use of patient-specific cutouts and bolus to achieve favourable dose distribution to the target volume [45]. However, due to the time-consuming and complicated setup of electron therapy, it is not frequently used.

Efforts have been made to explore the possibility of modulated electron radiotherapy, in which the energy and intensity of electron beams are modulated using MLC [15,30,32]. Using photon MLC for electron beam modulation allows the combination of both modalities in the same plan, but removing the electron applicator requires modifications in the traditional setup to restore the penumbra of the electron beam. Karlsson *et al*. (1999)

attempted to replace the air in the treatment head with helium to reduce the effect of electron scattering in the air. The experiment successfully reduced the electron penumbra width by more than 30 % [32]. Ma *et al*. (2000) developed a prototype of an electron MLC for MERT that could be attached to an electron applicator. They demonstrated the ability of MERT to provide uniform target coverage in a hypothetical treatment plan [45]. Al-Yahya *et al*. proposed using the few leaf electron collimator (FLEC) to deliver MERT in an automated manner. They showed that the FLEC could deliver MERT plans in a step-and-shoot mode at an SSD of 100 cm [4]. Alyahya *et al*. also presented an approach to combine MERT with IMRT. In this work, MERT was added to pre-optimized IMRT plans by reweighing the beam contributions and transferring some weights to electron energies [3]. Although many more approaches for MERT delivery have been suggested, unfortunately, the existing linac design is not optimized to modulate electron beam, which makes the practical implementation of MERT very challenging.

Mixed-Beam Radiotherapy (MBRT)

Mixed electron-photon beam radiotherapy is a technique that combines the use of electron and photon beams in a single treatment. Electrons and photons exhibit different behaviours on energy deposition. The depth dose curve of electron beams drops off very rapidly after reaching the maximum dose and the particles have a much shorter range compared to photons. In contrast, photon beams can penetrate deeper into human tissues due to their slower dose fall-off. The percent depth dose (PDD) curve for a 6 MV photon beam and a 6 MeV photon beam is shown in Fig. 1.5 for comparison. In a mixed-beam plan, the short-range electron beams target superficial cancer cells and the penetrating

photon beams kill deeper targets. The technique makes use of the advantageous characteristics of both particles and could be well-suited to treat superficial cancer with some deep-seated components [49].

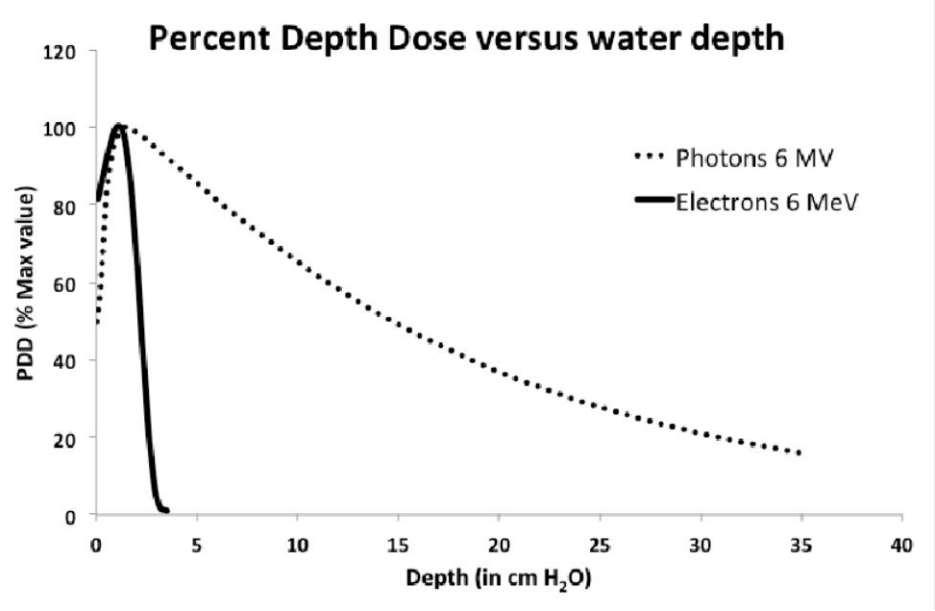

Figure 1.5: The PDD curve for a 6 MV photon beam and a 6 MeV electron beam in water [39].

Early in 1998, Janson *et al*. compared the performance of using mixed electron-photon beams and photon beams in a loco-regional radiotherapy plan for breast cancer patients after surgery [30]. The electron beam was shaped with a photon MLC and had an SSD of 85 cm. The study found that using a mixed-beam plan significantly reduced the dose to OARs compared to a conventional photon-only plan. However, it also resulted in a slightly inadequate dose to target volumes. Mu *et al*. (2004) studied the use of the mixed-beam technique to treat head and neck cancer patients [38]. It was also shown that the mixed-beam plan contributed to a lower healthy tissue dose compared to a photon IMRT plan. Alexander *et al*. investigated the possibility of combining FLEC-based MERT with

photon beams. The shape and weights of the FLEC apertures were first optimized using direct aperture optimization (DAO). Two tangential MLC-collimated photon beams were then added to the MERT plan and the plan was re-optimized to become an MBRT plan. The results showed that the addition of photon beamlets improved both target homogeneity and OAR sparing [6]. Mueller *et al*. (2017) developed a Monte Carlo based treatment planning process for MBRT and compared the plan quality among MBRT, MERT, IMRT and VMAT for a chest wall case and a squamous cell carcinoma case [49]. In both cases, the MBRT plan provided the best OARs sparing. Renaud *et al*. (2017) developed a mixed-beam optimization model and examined the performance of MBRT, MERT, and IMRT [57]. Again, the MBRT plan resulted in superior target coverage and OARs sparing.

Being able to deliver excellent dose distribution, an MBRT plan consists of many components. In the study by Mueller *et al*. (2017), an MBRT plan can comprise more than fifty apertures across five different beam energies. Due to the differing scattering properties of photons and electrons, the couch position also may need to be adjusted during the treatment for suitable SSDs.

1.2 Quality Assurance in External Beam Radiotherapy

Quality assurance is an essential process in radiotherapy that ensures the quality and safety of the treatment plan to be delivered. In this section, we summarize the procedures for patient-specific quality assurance in conformal radiotherapy.

1.2.1 Patient-specific Quality Assurance

Highly conformal radiotherapy is achieved by sharp dose fall-off. The use of steep dose gradients requires a much higher accuracy in both treatment planning and delivery. Involving a rotating gantry and dynamic MLC in the delivery also makes the process more complex and prone to errors. Therefore, patient-specific quality assurance (PSQA) must be performed for each plan individually before treatment to detect any potential uncertainties in radiation delivery. PSQA is often conducted by comparing the "reference" dose, the desired dose distribution, to the "evaluated" dose, the actual dose distribution delivered. The desired dose distribution is planned using the treatment planning system (TPS) according to defined objectives and constraints. The actual dose distribution can be acquired through various approaches, for instance, dose measurement in a phantom or log file-dose reconstruction. If the deviation between the two distributions is beyond the tolerance limit, the treatment quality is considered unacceptable, and the delivery system should be re-investigated [47].

1.2.2 Gamma Analysis

To ensure accurate delivery, the agreement between the planned and the actual dose distribution is assessed using gamma analysis. The dose comparison can be broken into two parts, the dose difference (DD) test and the distance-to-agreement (DTA) test.

The dose difference is a straightforward concept defined by the numerical difference δ between the reference dose D_e and the evaluated dose D_r at a given position $\vec{r}$:

$$\delta(\vec{r}) = D_e(\vec{r}) - D_r(\vec{r}) \tag{1.1}$$

This test is the most applicable in low-dose gradient regions where the dose level remains relatively constant with the position. However, in high-dose gradient regions, an acceptable small spatial shift can result in a significant dose difference falling outside the acceptance criteria. Therefore, the concept of DTA is introduced and defined as the nearest distance between a point $\vec{r_e}$ in the evaluated distribution and a point $\vec{r_r}$ in the reference distribution where $D_e(\vec{r_e}) = D_r(\vec{r_r})$ [68].

Taking into account both the dose difference and the distance-to-agreement, the gamma Γ is defined as [43]:

$$\Gamma(\vec{r_e}, \vec{r_r}) = \sqrt{\frac{r^2(\vec{r_e}, \vec{r_r})}{\Delta d^2} + \frac{\delta^2(\vec{r_e}, \vec{r_r})}{\Delta D^2}} \tag{1.2}$$

where $r(\vec{r_e}, \vec{r_r})/\Delta d$ and $\delta^2(\vec{r_e}, \vec{r_r})/\Delta D$ is the normalized DTA and DD respectively. The gamma index, the parameter for dose validation, is defined to be the minimum gamma for all evaluated points:

$$\gamma(\vec{r_r}) = min\left\{\Gamma(\vec{r_e}, \vec{r_r})\right\} \forall \left\{\vec{r_e}\right\} \tag{1.3}$$

A point that satisfies the condition of $\gamma < 1$ means it passes the specified criteria. The gamma passing rate (%) indicates the percentage of the evaluated points passing the test. For IMRT, commonly used QA criteria will be 3%/3 mm with a 90% passing rate [24].

1.2.3 Patient-specific QA Methods

The dose to be evaluated can be obtained via various techniques. Single-point measurement can be performed using an ionization chamber. Film dosimetry, electronic portal imaging devices (EPID), and diode array allow 2D dose measurement. Log file-based QA is an emerging method that provides quantitative information on treatment quality and enables the reproduction of 3D dose distribution.

Ionization Chamber

In a point-dose measurement, the ionization chamber is typically inserted in a QA phantom that is designed to mimic the patient's anatomy. The phantom provides attenuation that is consistent with human soft tissue and allows dose measurement at the target volume depth. The accuracy of point-dose measurement using an ion chamber depends on the position and the volume of the device. The chamber should be positioned in a region of uniform dose where the maximum and minimum dose inside the detector volume should not differ from the mean dose by more than 5 % [47]. In general, a chamber with a cavity smaller than 0.125 cc is suggested for IMRT measurement to maintain accuracy [25]. However, a smaller chamber volume also leads to a lower signal [22]. According to the measurement performed by Levbovich *et al.*, a 0.009 cc chamber is 60 times less sensitive than a 0.6 cc chamber [41]. Charge leakage should also be taken care of when a smaller chamber is used.

Film Dosimetry

Radiographic and radiochromic films are convenient dosimetric tools to obtain 2D dose distribution of extraordinary spatial resolution. Film can be easily placed inside various types of phantoms at any depth of interest. The dose information recorded on the film is expressed in terms of optical density (OD), which describes the degree of blackening of the film and can be measured by a densitometer [53]:

$$OD = log_{10}(\frac{I_0}{I}) \tag{1.4}$$

where I_0 is the measured initial light intensity of the incident beam in the absence of film and I is the intensity transmitted perpendicularly through the film. With a calibration curve, the absorbed dose can be converted from OD.

To calibrate a film properly, one should ensure that the dose delivered over a region of interest (ROI) in the calibration is uniform. A calibrated linac or Co-60 unit can be used to perform accurate film calibration. [52]. It was also suggested that the radiation beam used for calibration should share similar energy characteristics to the one used in experimental conditions to minimize the difference in energy response [46]. Besides, factors including beam energy, field size [61], film plane orientation [58], and film processing can all affect the dependence of OD on the dose. These measurement uncertainties should be taken into consideration to avoid dosimetric errors.

Electronic Portal Imaging Devices (EPID)

Electronic Portal Imaging Devices are imaging systems that measure the x-rays intensity of the exiting treatment beam. They are large, high-resolution 2D diode arrays attached to the gantry that capture exit dose images at all gantry angles (Fig. 1.6). Since it is positioned at the direct opposite of the gantry head, it is an excellent pre-treatment QA tool to validate the linac performance in terms of the dose output, beam homogeneity, as well as MLC leaf positions or trajectories. To compare the planned and the actual dose distribution in EPID-based PSQA, one can directly compare the 2D dose plane at the level of the detector [66]. Another more advanced strategy will be reconstructing the 2D or 3D dose distribution with the acquired portal images at all angles.

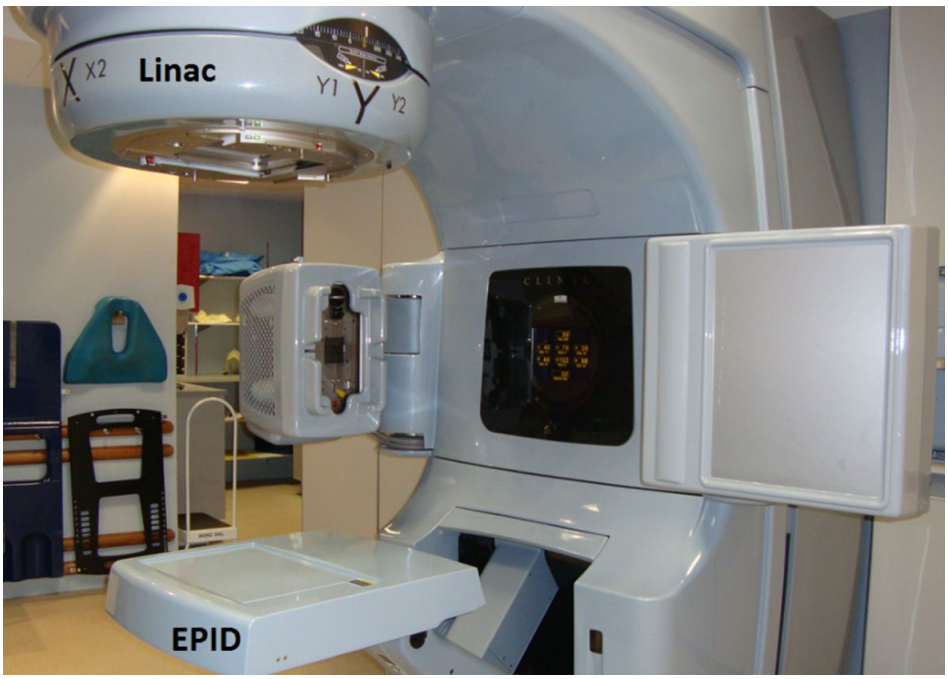

Figure 1.6: A Varian linac with an electronic portal imaging device (EPID) [11].

Diode Array

Diode arrays are electronic systems that contain an assembly of diodes in a single package. Depending on the arrangement and the positions of the diodes, they can measure either 2D or 3D dose distributions. Commercially available diode array systems are manufactured in different shapes for various purposes. Two commonly used diode arrays are ArcCHECK (Sun Nuclear, Melbourne, FL) and MapCHECK 2 (Sun Nuclear, Melbourne, FL). The ArcCHECK device is a cylindrical phantom with a helical detector grid of 1386 diode detectors and is often used for 3D dose measurement [63]. The MapCHECK 2 is a planar diode array of 1,527 diode detectors for 2D dose measurement [59]. Dose distribution measured with a diode array can be conveniently imported into QA software for dose verification, making it an efficient method with virtually no post-processing time.

Log File Analysis

During a treatment, the linac system records the axis positions and MU delivered at each control point. The data is then exported as a treatment log file after the delivery. From the log file, the difference between the expected and the actual positions of the MLC leaves, gantry angle, and MU can be analyzed directly, which makes it easier to identify the problematic control points. Besides, the detailed axis information at each delivery angle can be retrieved from the log file for dose reconstruction. The delivery data can be used as input for Monte Carlo (MC) dose simulation to estimate the 3D dose distribution in the patient's anatomy. With the reconstructed dose distribution, dose-volume histograms (DVHs) can be generated to examine the delivery quality.

1.3 Thesis Motivation and Objectives

As discussed previously, mixed-beam therapy is an emerging treatment modality that can provide excellent target coverage and normal tissue sparing to superficial cancer. However, being a newly developed technique, the QA procedures for MBRT have yet to be well-established. The objective of this study is to develop a comprehensive QA protocol for mixed-beam therapy which paves the way for the implementation of MBRT in clinical practice.

To design a QA program for MBRT, the plan verification methods should be able to detect errors that are specific to MBRT. The photon delivery of MBRT shares similar properties to IMRT and VMAT. However, in the electron delivery, MBRT uses photon MLC to modulate electron beams. The removal of the electron applicator makes the delivery more challenging as the photon MLC is not ideal for electron beam collimation. The effect of electron scattering in air may deteriorate the quality of the treatment. The use of multiple beam energies and the changing couch position in MBRT also create more room for error. Therefore, a well-designed PSQA program is essential to prevent any potential errors in the delivery of an MBRT treatment.

The performance of two PSQA methods was investigated in this study, they are log file-dose reconstruction and MapCHECK dose measurement. Log file analysis provides knowledge on the machine performance in the treatment. Log files contain quantitative details of the delivery and enable direct comparison between the expected and the actual delivery parameters. Since the data in the log files are independent of any factors external to the linac, any deviations between the planned and the reconstructed dose distribution

can be attributed to machine failures. On the other hand, MapCHECK measurement incorporates the potential setup uncertainties in the treatment. From the results measured by the MapCHECK, we can gain some insights into the errors that might occur when a real patient is being treated on the couch. Errors in phantom positioning and beam quality, including beam symmetry and flatness, can only be detected with a measurement-based QA method. The two methods together can be the basis of an inclusive MBRT PSQA program.

The project can be divided into two parts:

- Collect treatment log files upon deliveries of MBRT plans and reconstruct the delivered dose distribution in the patient anatomy using the EGSnrc Monte Carlo system. The Monte Carlo phantom of the patient on EGSnrc was obtained by conversion from the CT slices of the patient. The reconstructed dose to the CTV and OARs was compared to that of the planned dose.

- Deliver MBRT plans to the MapCHECK with collapsed gantry angle. The expected dose to the MapCHECK was simulated using the EGSnrc Monte Carlo system. A MapCHECK Monte Carlo phantom was modelled on EGSnrc for simulation according to the device blueprint provided by the manufacturer. The agreement between the measured and simulated dose distribution was evaluated using gamma analysis.

Chapter 2

Theory

This chapter explains some principles of radiation physics. The first part reviews the mechanics of particles interacting with matter and different forms of energy deposition. In the second part, we will talk about the basics of Monte Carlo dose calculation in radiotherapy. A brief introduction to the EGSnrc Monte Carlo system will also be given at the end of the chapter.

2.1 Particle Interactions in Radiation Therapy

Radiation energy is deposited into the patient's body through direct or indirect ionization. When sufficient kinetic energy is transferred from the radiation to a bound electron, the electron can overcome the attractive force from the nucleus and escape from the atom. The formation of a positive ion in this process is known as ionization. Charged particles like electrons interact with matter and result in direct ionization. Uncharged particles like photons cause indirect ionization by interacting with matter to produce charged particles

which subsequently causes ionization. In this section, we review the theory behind the interactions of electrons and photons with matter.

2.1.1 Interactions of Electrons with Matter

As charged particles, electrons experience Coulomb interactions with the absorber atoms when travelling through an absorbing medium. The types of Coulomb interactions that occur depend on the relative size of the atomic radius a of the absorber atom and the impact parameter b, which is the perpendicular distance between the nucleus and the initial path of the incident particle (Fig. 2.1). When $b \approx a$, the incident electron directly impacts with an orbital electron of the absorber atom and hard collision occurs. Each hard collision involves a relatively large amount of energy transfer between particles. When $b \gg a$, the incident electron interacts with the bound electrons of many atoms and undergo a series of soft collisions. Despite the small energy transfer in each soft collision, the total energy loss by the incident electron in soft collisions is large due to a large number of interactions. When $b \ll a$, the incident electron interacts with the nucleus of an absorber atom and is deflected by its strong electric field. The deflected electron experiences a sudden deceleration and loses kinetic energy with the emission of bremsstrahlung photons. This process is called radiative collision.

When moving across an absorbing medium, the charged particle transfers its kinetic energy to either the medium through collision loss or bremsstrahlung photons through radiation loss. The rate of energy loss per unit mass length, expressed in g cm^{-2}, by the

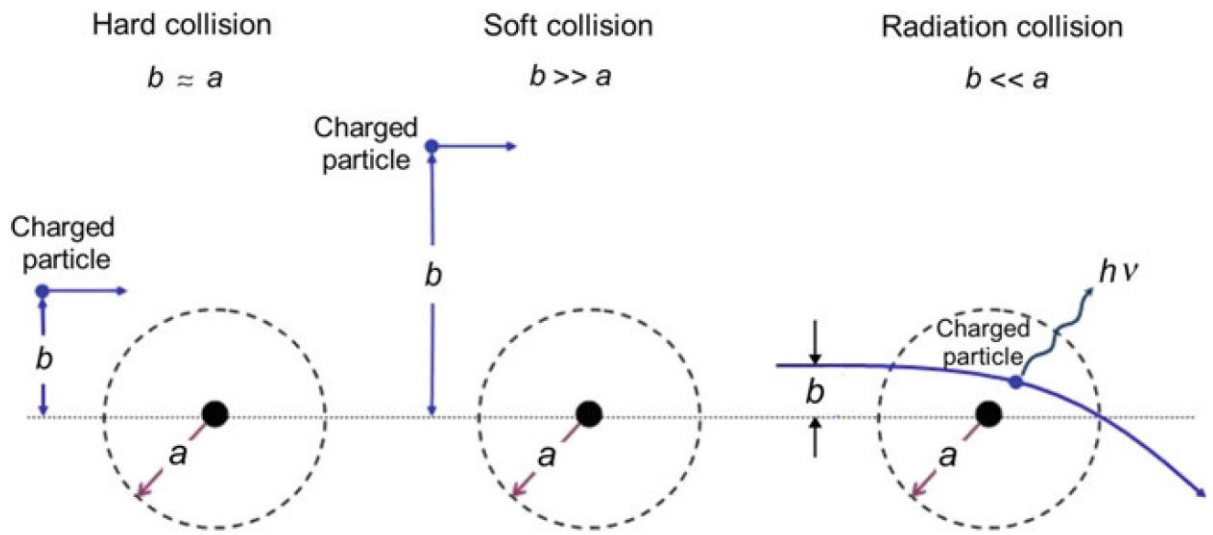

Figure 2.1: The three categories of Coulomb interactions between an electron and an atom [55].

travelling electron in the medium can be described by the mass stopping power S (in MeV cm^2 g^{-1}) :

$$S = -\frac{1}{\rho}\frac{dE}{dx} \tag{2.1}$$

where ρ is the density of the absorber. The total mass stopping power of an electron can be broken down into the radiation component and electronic component. For computational convenience, the electronic component is further divided into soft and hard collision. The total mass stopping power can be expressed using the following equation:

$$S_{tot} = S_{rad} + S_{col}^{soft} + S_{col}^{hard} \tag{2.2}$$

Radiation Stopping Power

According to the Larmor relationship, the power of bremsstrahlung emission of a charged particle is proportional to the square of its acceleration *a*. For a particular atomic number *z* and mass *m* of the incident charged particle, its acceleration is linearly proportional to the atomic number *Z* of the absorbing medium. The total cross section for bremsstrahlung emission has been shown by *Hans Bethe* and *Walter Heitler* in 1930s to be [14]:

$$\sigma_{rad} \propto \alpha r_e^2 Z^2 (cm^2/nucleus) \tag{2.3}$$

where α is the fine structure constant, r_e is the classical electron radius. With the bremsstrahlung cross section, the mass radiation stopping power of an electron can be expressed as:

$$S_{rad} = N_a \sigma_{rad} E_i \tag{2.4}$$

where N_a is the atomic density, E_i is the initial total energy of the electron.

Collision Stopping Power

Compared to heavy charged particles, the relativistic effects in the collision between the incident electron and orbital electrons become more significant due to the low mass of electrons. Colliding with orbital electrons can also result in up to 50% of energy loss by the incident electron. Combining the effect of both soft and hard collision, the complete mass collision stopping power for electrons is given by the ICRU Report 37 as:

$$S_{col} = 2\pi r_e^2 \frac{Z}{A} N_A \frac{m_e c^2}{\beta^2} \left\{ ln\frac{E_K^2}{I^2} + ln(1+\frac{\tau}{2}) + F^-(\tau) - \delta \right\} \tag{2.5}$$

where $\tau = E_K/(m_e c^2)$, $\beta = v/c$ and δ is the density effect correction. $F^-(\tau)$ is a function for electron and is equal to:

$$F^-(\tau) = (1-\beta^2)[1 + \frac{\tau^2}{8} - (2\tau+1)ln2] \tag{2.6}$$

The relationship between the mass stopping powers and the kinetic energy for electrons is illustrated in Fig.2.2.

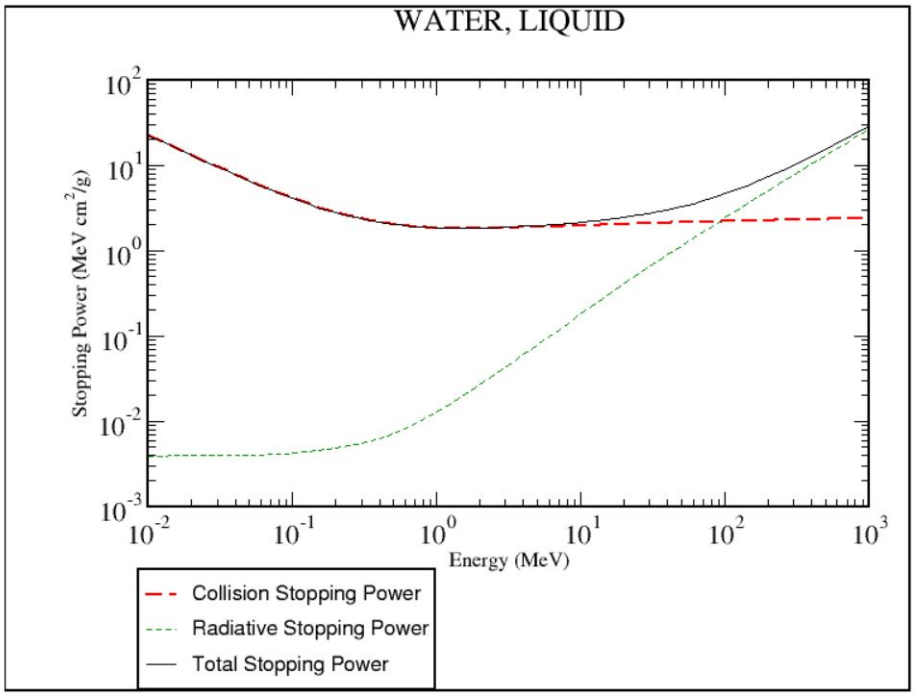

Figure 2.2: The mass stopping powers for electrons in water as a function of electron kinetic energy [13].

Range of Electrons

When travelling through a medium, electrons experience a large number of collisions that result in deflections and kinetic energy loss. Due to their small mass, electrons are more likely to be scattered with large scattering angles and move in a tortuous trajectory. Therefore, instead of the penetration depth, various ranges of interest in radiotherapy and dosimetry were defined for electrons. These electron ranges are identified on the percent depth dose curve for electrons (Fig. 2.3). Besides, the range of electrons can also be defined by its mean path length in the absorber, called the "continuous slowing down approximation (CSDA)" range. This concept can be mathematically expressed as:

$$R_{CSDA} = \int_0^{(E_K)_0} \frac{1}{S_{tot}(E)} dE \tag{2.7}$$

where $(E_K)_0$ is the initial kinetic energy of the electron, and $S_{tot}(E_K)$ is the total mass stopping power of the electron as a function of its kinetic energy E_K.

2.1.2 Interactions of Photons with Matter

When travelling through an absorber, a photon interacts with the nuclei or the orbital electrons of the absorber atom in several ways. As a result of interactions, charged particles are often released by gaining energy from the incident photon. The progressive reduction of photons' energy as it traverses a medium is known as attenuation, which can be characterized by a parameter called the linear attenuation coefficient μ. The relationship between the intensity I of a narrow beam of mono-energetic photons and its travelling distance x in a medium can be expressed as:

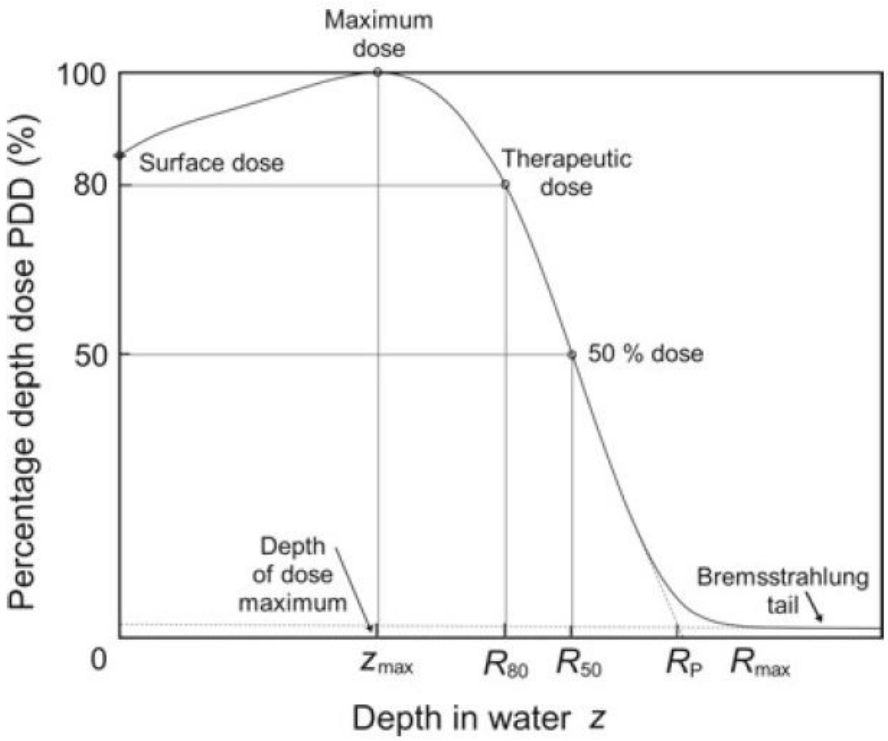

Figure 2.3: A typical percentage depth dose curve of electron and some common definitions of electron range, including R_{80}, R_{50}, R_P, R_{max} [55].

$$I = I_0 e^{-\mu x} \tag{2.8}$$

where I_0 is the initial intensity of the incident photon beam. The parameter μ is dependent on the incident photon energy $h\nu$ and the atomic number Z of the medium. It describes the probability of an interaction occurring between the photon and the absorber atom per unit path length. To remove the dependence on material density, the mass attenuation coefficient, $\mu_m = \mu/\rho$ is more often used for convenience.

Determined by the types of interaction with the absorber atom, photons are either absorbed or scattered. In the following, some interactions of major importance in medical physics will be introduced.

Compton Scattering

Compton scattering (incoherent scattering) occurs in the interaction between a photon and a loosely bound orbital electron of an absorber atom. An electron is loosely bound if its binding energy E_B is smaller than the photon energy $h\nu$. In Compton scattering, an incident photon of energy $h\nu$ strikes a stationary orbital electron and is scattered at an angle θ with energy $h\nu'$. Upon interaction, the electron acquires energy from the photon and is ejected at a recoil angle of ϕ (Fig. 2.4).

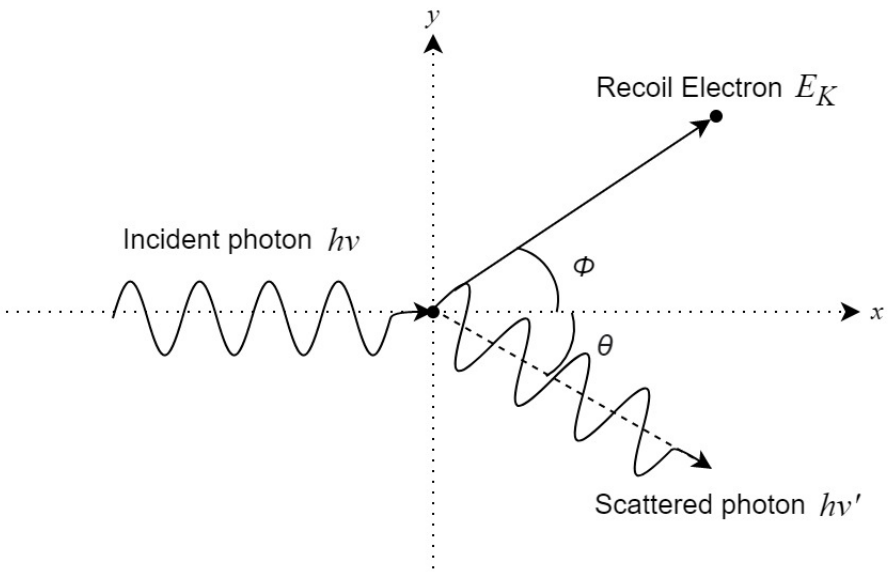

Figure 2.4: The schematic diagram of Compton scattering.

The scattering angle ranges from 0°(forward scattering) to 180°(back scattering), and the recoil angle ranges from 0°to 90°. Applying the conservation laws of energy and momentum, the relation among $h\nu$, $h\nu'$, E_K and θ is derived as:

$$E_K(h\nu, \theta) = h\nu - h\nu' = h\nu \frac{\epsilon(1 - cos\ \theta)}{1 + \epsilon(1 - cos\ \theta)} \tag{2.9}$$

where $\epsilon = \frac{h\nu}{m_e c^2}$.

The cross-section for a Compton interaction to occur between a photon and an electron per unit solid angle can be expressed as the Klein-Nishima differential electronic cross section per unit solid angle $d_e\sigma_C^{KN}/d\Omega$. Consequently, the Klein–Nishina electronic cross section (in cm^2/electron) is derived by integrating $d_e\sigma_C^{KN}/d\Omega$ over one whole solid angle:

$$ {}_e\sigma_C^{KN} = \int \frac{d_e\sigma_C^{KN}}{d\Omega} d\Omega \tag{2.10} $$

The probability for a Compton interaction to occur for an atom can be characterized by the Klein–Nishina Compton atomic cross-section ${}_a\sigma_C^{KN} = Z({}_e\sigma_C^{KN})$. From ${}_a\sigma_C^{KN}$, the Compton mass attenuation coefficient σ_C/ρ is calculated:

$$ \frac{\sigma_C}{\rho} = \frac{N_A}{A}({}_a\sigma_C^{KN}) = \frac{ZN_A}{A}({}_e\sigma_C^{KN}) \approx \frac{1}{2}N_A({}_e\sigma_C^{KN}) \tag{2.11} $$

where N_A is the Avogadro number.

Rayleigh Scattering

When an incident photon interacts with an absorber atom as a whole without causing excitation or ionization, Rayleigh scattering (coherent scattering) occurs. Due to its large mass, the absorber atom takes up an insignificant amount of recoil energy from the photon and the incident photon is scattered at a relatively small scattering angle with no energy loss. This type of interaction is more likely when the incident photon energy $h\nu$ is low and the atomic number Z of the absorbing medium is high.

The Rayleigh mass attenuation coefficient σ_R/ρ can be obtained through the relationship:

$$\frac{\sigma_R}{\rho} = \frac{N_A}{A}({}_a\sigma_R) \tag{2.12}$$

where ${}_a\sigma_R$ is the Rayleigh atomic cross section that is proportional to $Z^2/(h\nu)^2$.

Photoelectric effect

The photoelectric effect is the interaction between a photon and a tightly bound orbital electron of an absorber atom. A tightly bound electron has a binding energy E_B comparable to or slightly smaller than the photon energy $h\nu$. In a photoelectric effect, a photon with energy $h\nu$ hits an orbital electron and is then completely absorbed. The electron which absorbed the photon is ejected as a photoelectron with kinetic energy $E_K = h\nu - E_B$. Subsequently, the vacancy of the ejected electron is filled by another electron from the outer shell. The energy from the electronic transition will be released either as a characteristic x-ray (Fig. 2.5) or an Auger electron.

The mass attenuation coefficient for the photoelectric effect τ/ρ can be calculated from the atomic cross section ${}_a\tau$ with the equation:

$$\frac{\tau}{\rho} = \frac{N_A}{A}({}_a\tau) \tag{2.13}$$

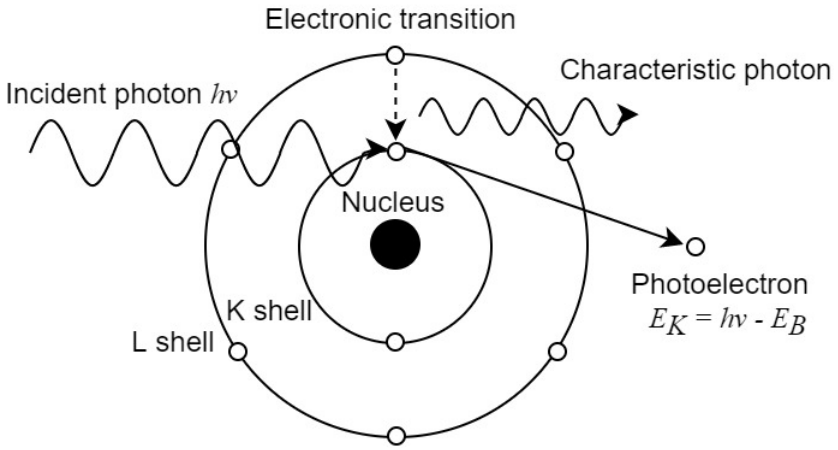

Figure 2.5: The schematic diagram of photoelectric effect and the subsequent emission of a characteristic photon.

Pair Production

When an incident photon has energy higher than the total rest energy of an electron and a position (i.e. $h\nu > 2m_e c^2$), the photon can disappear and materialize into an electron-position pair. This direct conversion of light energy into matter is called pair production. For the phenomenon to occur, the conservation laws of energy, charge and momentum must be satisfied. Therefore, pair production only takes place in the vicinity of a third particle, either an atomic nucleus or an orbital electron in the absorber, which can take up the momentum of the incident photon. When pair production occurs in the Coulomb field of an electron, the extra energy and momentum absorbed by the orbital electron may be sufficient for it to escape the interaction site. Since two electrons and one position are generated in the process, it is more often known as triplet production.

The atomic cross-section ${}_a\kappa$ for pair production can be derived by:

$$ {}_a\kappa = \alpha r_e^2 Z^2 P(\epsilon, Z) \tag{2.14}$$

where $P(\epsilon, Z)$ is a function of $h\nu$ and Z. The mass attenuation coefficient for pair production κ/ρ can be expressed in terms of ${}_a\kappa$ with the equation:

$$\frac{\kappa}{\rho} = \frac{N_A}{A}({}_a\kappa) \tag{2.15}$$

Attenuation coefficients

The total mass attenuation coefficients μ_m of a photon travelling in an absorbing matter can be calculated by summing up the corresponding mass attenuation coefficients for the four effects:

$$\mu_m = \frac{\mu}{\rho} = \frac{\sigma_C}{\rho} + \frac{\sigma_R}{\rho} + \frac{\tau}{\rho} + \frac{\kappa}{\rho} \tag{2.16}$$

The likelihood of an individual effect happening depends on the atomic number Z[1] of the absorber and the energy $h\nu$ of the incident photon. Therefore, a particular process will be predominant within a certain range of Z and $h\nu$ as shown in Fig. 2.6.

2.2 Monte Carlo simulations in radiotherapy

The Monte Carlo (MC) dose calculation method has been considered the ”gold standard” in radiotherapy dosimetry due to its accuracy and ease of use. Some available Monte Carlo code systems that are frequently used in the field of medical physics include EGSnrc [34], PENELOPE [9], GEANT4 [2] etc. The MC method simulates the physical

[1]The probability also depends on the atomic mass number A but the dependence is waeker because of the limited Z dependence of the ratio Z/A.

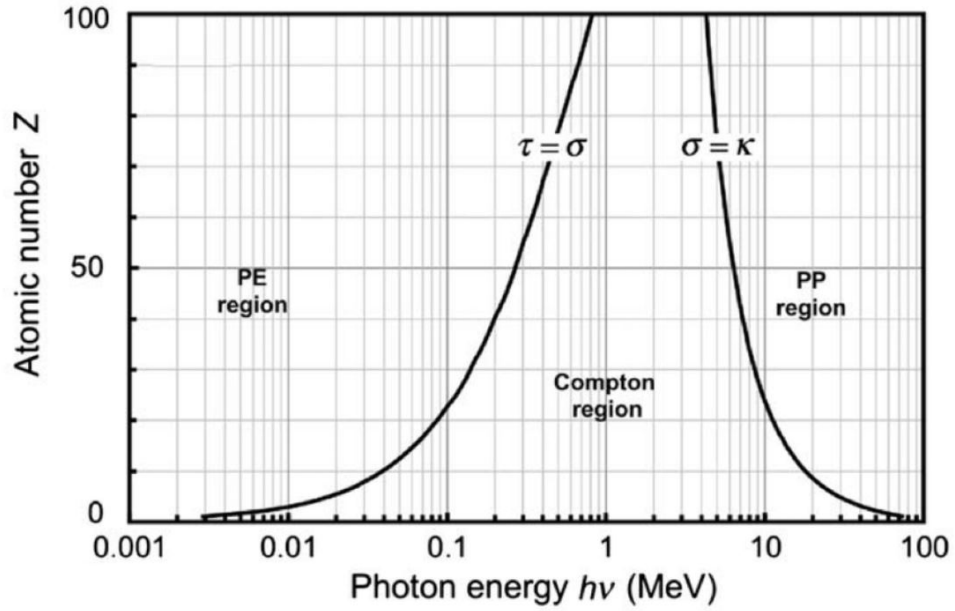

Figure 2.6: The region of predominance for photoelectric effect, Compton effect, and pair production in the plot of Z versus $h\nu$ [1].

process of particle interactions without the need for complex approximations. Due to its stochastic nature, high dose precision can be simply achieved by providing a sufficient amount of simulated particles [48]. This section provides a brief introduction to the working principle of MC simulations and discusses the clinical aspects of the MC method in handling particle transport in accelerators and patients.

2.2.1 The Monte Carlo Method in Dose Calculation

In a Monte Carlo simulation, the interactions of all incident particles and secondary particles are simulated. First, the nature and entering direction of primary particles are determined by the model of the source. After travelling a certain distance, each particle undergoes interaction according to the probability distribution. Then, the particles are either absorbed or scattered to the next interaction site with updated energy and direction.

If the energy or the position of a particle lies beyond the range of interest, the particle is discarded [35]. For neutral particles like photons, the process of particle transport can be described by an analog simulation which consists of four steps [18]:

Step 1, determine the travelling distance r of the particle before the next interaction. The random distance r is sampled according to a probability distribution $p(r)$ using the inverse transform method:

$$r = -\frac{ln(1-\xi)}{\mu} \tag{2.17}$$

where ξ is a random number which has a uniform distribution between 0 and 1 and is equal to the cumulative probability of $p(r)$:

$$\int_0^r p(r')dr' = \xi \tag{2.18}$$

with $p(r)dr$ being the differential probability to find a particle in the interval $[r, r+dr]$, which is dictated by exponential attenuation with attenuation coefficient μ.

Step 2 is to transport the particle to the interaction site. According to the geometric information of the simulation volume, the particle's trajectory is simulated.

Step 3, decide the type of interaction. The total cross-section σ_{tot} is equal to the sum of all cross-section σ_i for interaction type i, i.e. $\sigma_{tot} = \sum \sigma_i$. To sample the interaction type, a random number ξ is compared to a ratio of cross-sections. For example, if $\xi < \sigma_1/\sigma_{tot}$, interaction type 1 will be selected. Likewise, interaction type 2 will be selected if $\xi < (\sigma_1 + \sigma_2)/\sigma_{tot}$.

Step 4, simulate the selected interaction with the physics of particle collision and calculate the new energy and direction of the particle. Then, the four steps are repeated for each particle until it ”dies”. For photons, their trajectory ends due to pair production or photoelectric effects, or when their energy becomes lower than the specified low-energy photon cutoff (PCUT) due to scattering.

For charged particles like electrons, they experience a large number of interaction before their energy reaches the low-energy cutoff (ECUT). Analog simulation, which is often referred to as an ”event-by-event” approach, is not practical for charged particles and therefore, the condensed history (CH) technique, pioneered by Berger [5], is used instead. By assuming that the change in electron energy or direction in most interactions were insignificant, several interactions are grouped in to a single ”condensed history step” and the cumulative effect of multiple interactions were considered as a whole.

2.2.2 Treatment Head Simulation

To simulate the particles' trajectory from the treatment head to the patient, the particles are transported from the radiation source to various components, including the collimators, flattening filters and other patient-dependent structures such as jaws and MLCs. Due to the complexity of a linac, it is time-consuming to simulate the entire process for every single plan. Therefore, the simulation process is often split into several steps.

The simulation starting from electrons striking the target or the scattering foil to just before reaching the jaws in the linac head can be carried out separately, and the information will be stored into a ”phase-space” file [18]. Since this part of the simulation is mainly

determined by the structure of the accelerator but not the patient-specific treatment plan, the phase-space file can be reused for the beam of the same particle and energy generated by the same linac. With the pre-calculated phase-space file, one simply needs to simulate the particles downstream for each patient plan and make dose calculations more efficient. However, it is important that the number of particles in the phase-space file is large enough to minimize the uncertainty propagated to the downstream quantities.

2.2.3 Patient Dose Calculation

The simulated particles travelling through the patient-specific components will arrive at the patient phantom in which the patient dose is calculated. In most cases, the patient anatomy acquired from CT slices is converted into a computational phantom for calculation. The conversion is done using calibration curves relating the Hounsfield unit (HU) of the CT scan to material interaction coefficients [18]. The computational phantom contains information on the geometrical structure, material compositions and mass densities inside the volume of interest. The resolution of the dose distribution depends on the voxel size of the phantom.

Being a stochastic method, the accuracy of dose calculation is correlated to statistical uncertainty. A radiation history is referred to the entire process of an incident particle and its progeny particles traversing the medium and undergoing collisions until they are all eventually absorbed [19]. The statistical uncertainty of the scored quantity dose D, or the standard error $s_{\overline{D}}$ of the mean dose, can be expressed in terms of the number of histories

N [18]:

$$s_{\overline{D}} = \sqrt{\frac{1}{N-1}\left(\frac{\sum_{i=1}^{N} D_i^2}{N} - \left(\frac{\sum_{i=1}^{N} D_i}{N}\right)^2\right)} \tag{2.19}$$

where we can see that the uncertainty $s_{\overline{D}}$ is approximately proportional to $1/\sqrt{N}$. Since the simulation T is proportional to N, a longer simulation time is needed to achieve higher precision.

2.3 The EGSnrc Monte Carlo system

EGSnrc is a general-purpose toolkit released in 2000 by the National Research Council of Canada to perform Monte Carlo simulations of coupled electron and photon transport [35]. It can handle particles with energies ranging from a few keV up to hundreds of GeV. A main feature of the package is the use of the condensed history technique used for electron and positron transport, which approximates the cumulative effect of numerous transport and collision processes into a single path length. This method offers a lower threshold for computing power and better computing efficiency. This section briefly introduces the two EGSnrc user codes for beam modelling and dose calculation, BEAMnrc and DOSXYZnrc.

2.3.1 BEAMnrc

BEAMnrc is a Monte Carlo code to simulate beam sources for external radiotherapy. The simulation is instructed by the BEAMnrc inputs and component modules specified by the user.

The BEAMnrc input file (.egsinp) defines the parameters controlling the Monte Carlo transport and the nature of the incident particles in terms of their charge and type of source. The rest of the settings will be handled by the component modules' input files. In BEAMnrc, the accelerator is divided horizontally into several portions. Each of these portions is an independent component module that can be re-used in different simulations. This design allows users to change the parameter of each component separately without affecting the other settings. The patient-specific part of the simulation, including the position of the jaws and MLC, are controlled by the component modules files.

2.3.2 DOSXYZnrc

DOSXYZnrc is a Monte Carlo code to calculate 3-dimensional dose distribution in a computational phantom. It simulates particle transport in the phantom and scores the energy deposition in each voxel. The simulation parameter is controlled by the user using the DOSXYZnrc input file (.egsinp). The structure of the phantom is described by the egsphant (.egsphant) file.

The EGSnrc phantom for the simulation is specified in the DOSXYZnrc input file. The egsphant can either be derived from CT slices or manually defined by the user on the DOSXYZnrc GUI. The egsphant file defined the voxel number, the voxel boundaries, and the material and density at every voxel of the phantom. The input file also determines the phase-space data file and the beam source file to be used, with the isocentre and incident direction of the source for each control point described. When the simulation is completed, a .egslog file and .3ddose are generated as the output. The .egslog file contains

information regarding the statistical data, number of histories and computational time of the simulation. The .3ddose file recorded the dose and the statistical uncertainty to every single voxel in the phantom.

Chapter 3

Materials and Methods

The feasibility of two possible patient-specific quality assurance (PSQA) methods for mixed-beam radiotherapy (MBRT) was examined in this study. This chapter discusses the methodologies adopted to evaluate the performance of log file-based and MapCHECK-based quality assurance. The details of the two approaches will be considered in separate sections.

3.0 The Brems platform

In this project, an in-house web-based treatment planning system, Brems, was used. After a plan is optimized on Brems, the plan .xml file can be downloaded and imported to the linac for delivery. The .xml contains the parameter for linac operations and can be used in the developer mode of Varian TrueBeam linacs. Brems also handles dose simulation and dose processing. The 3D dose distributions obtained from simulations can be displayed on the patient CT, and dose DVH and dose profile can be plotted. From the simulated

dose data, one can perform dose arithmetic and normalization on Brems. The processed dose then can be exported as DICOM files which can then be read in other softwares.

3.1 Log file-based Quality Assurance

Log file analysis has been shown to be a viable method for IMRT and VMAT plan verification [20,21,33]. Since MBRT plans share similar natures with IMRT and VMAT, a similar QA approach could be applicable. In this study, we attempted to reconstruct the 3D dose distribution of MBRT plans for PSQA using the data provided in treatment log files. The detailed procedures to validate this method will be elaborated in this section.

3.1.1 Treatment plan and Delivery

An MBRT plan for a patient (patient 1) with soft tissue sarcoma (STS) in the right leg was robustly optimized. The plan consists of an arc delivery of a 6 MV photon beam, and step-and-shoot deliveries of 5 electron beam energies (Table 3.1). The SAD of the photon delivery was 100 cm, and that of the electron delivery was shortened to 80 cm to minimize the effect of electron scattering in the air. A CT slice of the patient and the position of the CTV are shown in Fig. 3.1. The delivery angles of the photon beam and the electron beams are indicated by the yellow arc and the white arrows, respectively.

Due to the changing couch position throughout the treatment, each energy component of an MBRT plan was delivered with a corresponding .xml plan file. In other words, the MBRT plan for patient 1 consists of six .xml plan files. The log files were also collected separately for each energy component. To evaluate inter-linac and intra-linac differences

Table 3.1: Summary of the MBRT plan for patient 1.

Particles	Energy	Angle	SAD (cm)
Photon	6X	From -50° to 170°	100
Electron	6E, 9E, 12E, 16E, 20E	(15°, 45°, 75°)	80

in deliveries, the whole plan was delivered one time on three Varian TrueBeam linacs (TB3, TB4, TB5) and ten times on TB5.

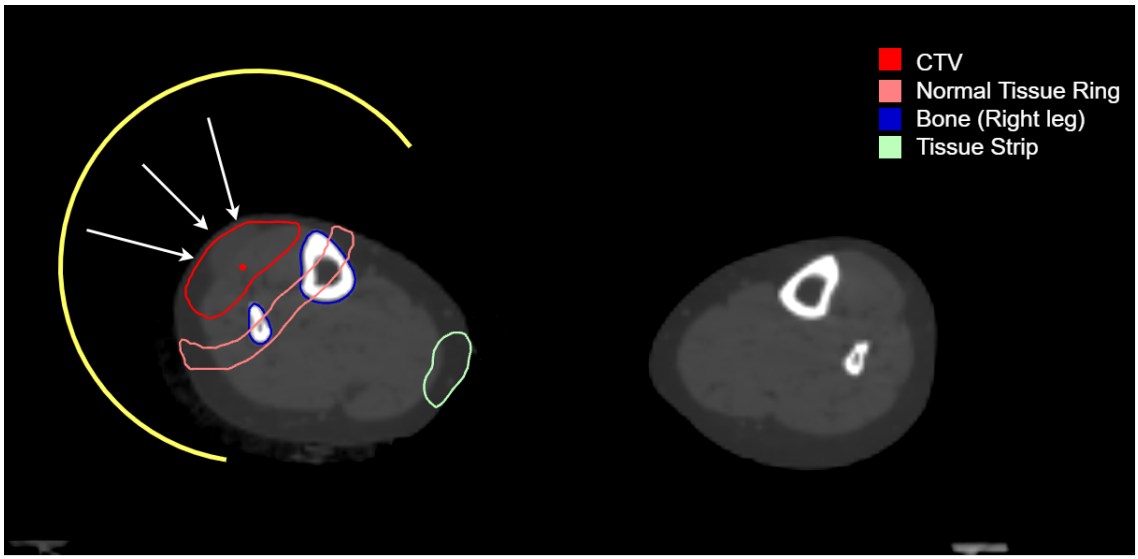

Figure 3.1: A CT slice of patient 1 with the contour of the CTV and three OARs. The yellow arc represents the photon's arc segment, while the white arrows represent the electron beam angles.

3.1.2 Log file Collections

During the delivery with the Varian TrueBeam linac, the actual axis positions and the corresponding number of MU delivered were recorded by the TrueBeam system at every 20 ms [67]. The collected information was stored in a trajectory log file which was generated upon the completion of each delivery. The data in the trajectory log files were read and

parsed with the log analyzer module of the Pylinac Library [36]. In order to perform dose recalculation, the following data of each control point were retrieved from the log file:

- Gantry angle
- Collimator angle
- Couch positions (horizontal, longitudinal, vertical directions)
- Couch angle
- MLC leaf positions (Bank A and B, each with 60 leaves)
- Jaw positions (x and y directions)
- MU

3.1.3 Log file-Dose recalculation

The dose calculation was performed with the Monte Carlo method using the EGSnrc code system. TrueBeam phase space files (TrueBeamPhsp) provided by Varian were used as the beam source. The axis data obtained from the log file were used to generate the input files for the MC simulation. The MLC leaf positions and jaw positions were defined in the BEAMnrc input files. The gantry angle, collimator angle, and the isocentre which was converted from the couch positions, were specified in the DOSXYZnrc files. An egsphant of the patient's anatomy was generated from the CT slices of the patient. The DOSXYZnrc user code was used to score the dose to the patient's anatomy with a voxel size of $2.5 \times 2.5 \times 2.5$ mm^3.

3.1.4 Dose Comparison

The planned and the log file-recalculated dose distributions were compared for each set of data. The mean dose to the CTV and the OARs, and the percentage difference between the planned and the recalculated values were calculated. Discrepancies in log file-recalculated doses obtained from deliveries across three different linacs were analysed. This analysis was also performed for the set of repeated deliveries on the same linac.

3.2 MapCHECK-based Quality Assurance

For the measurement-based PSQA for MBRT, we investigated the viability of using the MapCHECK 2 device (Sun Nuclear, Melbourne, FL) (Fig. 3.2). ArcCHECK has been a commonly used device (Sun Nuclear, Melbourne, FL) for IMRT and VMAT dose verification due to its capability to measure 3D dose distribution [8, 42, 51]. However, the ArcCHECK detectors are positioned at a physical depth of 2.9 cm, which is comparable to the range of 6 MeV and 9 MeV electron beams. Due to the steep dose fall off of electron beams, the signals from these energies measured by the ArchCHECK will be too low. Since low energy electron beams are often used in an MBRT plan, MapCHECK 2 with a physical detector depth of 1.2 cm (water-equivalent depth of 2 cm) is more favourable. This section explains the procedures to assess the practicability of using MapCHECK 2 for MBRT QA.

Figure 3.2: The MapCHECK®2 device (Sun Nuclear, Melbourne, FL) [59].

3.2.1 MapCHECK Detector Specifications

MapCHECK 2 is a two-dimensional planar dosimetry detector tool. It contains a 26 cm x 32 cm detector array consisting of 1527 solid state detectors. The position and arrangement of the detectors are shown in Fig. 3.3. The device can measure electron beams in the energy range of 6 MeV to 25 MeV and photon beams of energy ranging from Co-60 to 25 MV. Above the detector array, there is a 2 cm water-equivalent inherent buildup made of polycarbonate. MapCHECK 2 was accompanied by the Sun Nuclear Corporation® (SNC) patient software, which handled the calibration process and dose measurement. After each measurement, the system outputs a ”measurement text file” which records the absorbed dose to every detector on the array.

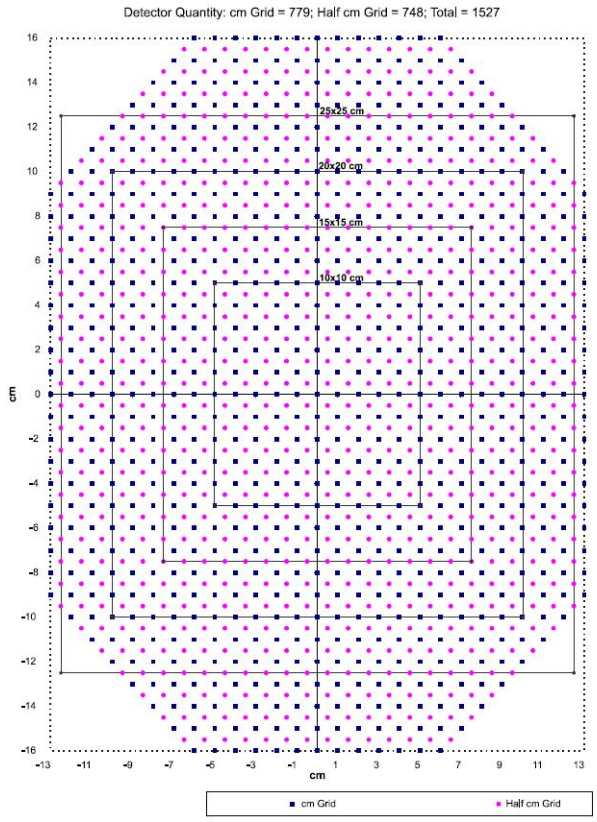

Figure 3.3: The geometry of the detector array [59].

3.2.2 Phantom Modelling

To validate the viability of MapCHECK-based QA, the dose distribution to the MapCHECK was calculated by Monte Carlo methods and compared to MapCHECK measurements. To perform a Monte Carlo dose simulation on the MapCHECK, a MapCHECK egsphant was created and the dose to each voxel in the phantom was calculated. For the best agreement between the Monte Carlo dose and the measured dose, the MapCHECK egsphant must be as realistic as possible. We attempted two different methods to model the MapCHECK phantom.

Generating MapCHECK Egsphant from CT

A straightforward way to generate the MapCHECK egsphant was through CT conversion. The MapCHECK was levelled and a CT scan was taken for the device. The CT slices of the MapCHECK were imported to the Eclipse treatment planning system (Varian Medical Systems, Milpitas, CA). With the Eclipse TPS, the case of the device and the silicon detectors were outlined using the automatic contouring tool, which allowed the user to select particular regions in the image according to a specified range of CT numbers. When converting the CT slices to an egsphant, the material and density in contoured volumes can be manually defined. The body contour of the MapCHECK was selected to be polycarbonate, with a density of 1.2 g/cm^3. The detectors' contour was chosen to be silicon which has a density of 2.33 g/cm^3. The egsphant generated from CT slices has a regular voxel size of 0.25 cm x 0.25 cm x 0.25 cm. For clarity, this egsphant will be referred to as the "CT MapCHECK egsphant" in the following text.

Generating MapCHECK using the Manufacturing Specification

Another method to generate the MapCHECK egsphant was to write the egsphant file manually according to the blueprint provided by the manufacturer. With the MapCHECK's dimension, configuration, and the detectors' position specified, the material and density in the MapCHECK phantom were defined voxel by voxel. Due to the irregular detectors' arrangement, the egsphant was built using unequal voxel sizes. This method allowed the phantom to be modelled in a more realistic manner with no assumptions on the composition based on CT numbers. However, it was more time-consuming to manually assign

material and density to each voxel. In contrast to the CT MapCHECK egsphant, this egsphant will be referred to as the ”blueprint-defined MapCHECK egsphant”.

3.2.3 MapCHECK Calibration

Array Calibration

Before doing measurements with the MapCHECK, array calibration is needed to account for the sensitivity difference across the detectors. The calibration process was carried out according to the instructions provided by the MapCHECK 2 Reference Guide [59]. In the calibration, the device was exposed to a 37 cm x 37 cm jaw-defined 6 MV photon field or a 25 cm x 25 cm 12 MeV electron field collimated by an electron applicator. The fields were delivered at 100 cm SSD. The exposure was repeated for multiple MapCHECK orientations. The reason for using separated array calibrations for photons and electrons was to minimize the effect of the energy dependence of the detectors. A calibration file for 6 MV and 12 MeV were generated after the calibration process and were later used to apply correction factors to the measurements. The experimental setup for MapCHECK calibration and measurement is shown in Fig. 3.4.

Absolute Dose Calibration

Absolute dose calibration allows the conversion from relative dose to absolute dose. The absolute dose calibration was carried out by delivering a 10 cm x 10 cm radiation field of each energy of interest to the array with the corresponding known absolute dose-to-water at the detector depth input into the SNC patient software. The beams were delivered at

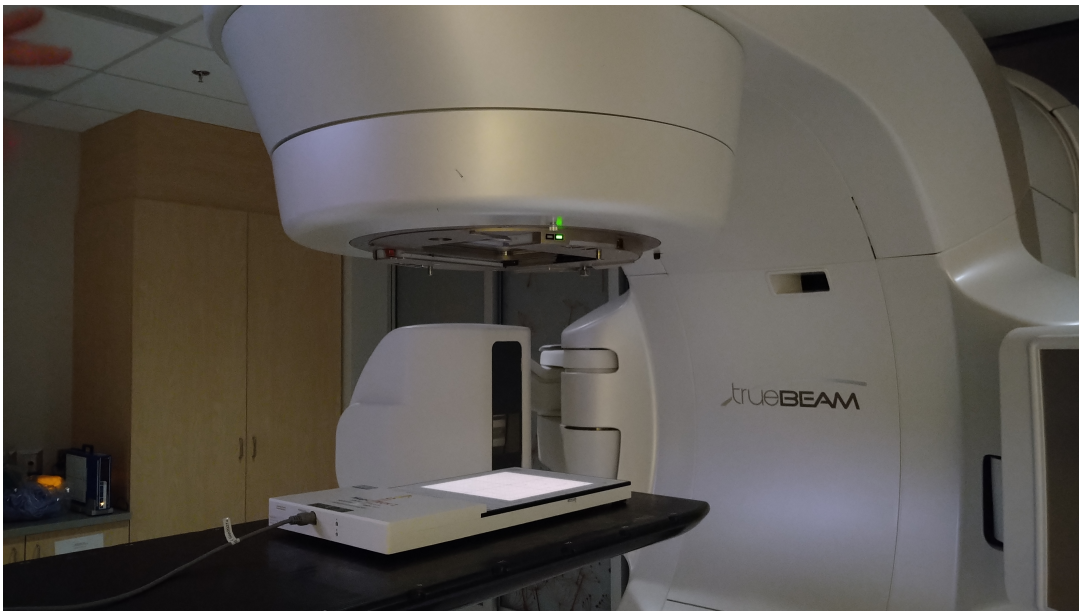

Figure 3.4: The setup for MapCHECK calibration and measurement.

an SSD of 100 cm. The MapCHECK was positioned such that the centre detector aligned with the central axis of the radiation field. The dose calibration was performed for a photon beam at 6 MV, and electron beams at 6 MeV, 9 MeV, 12 MeV, 16 MeV, and 20 MeV.

The expected dose-to-water $D_{water}^{Calibration}$ at the detector depth under the calibration condition was obtained by doing a Monte Carlo simulation on the blueprint-defined MapCHECK phantom. The Monte Carlo dose $D_{detector}^{MC}$ delivered to the voxel of the centre detector in the phantom was retrieved from the output dose file (.3ddose file). The MC dose-to-detector $D_{detector}^{MC}$ was first converted to the MC dose-to-water D_{water}^{MC} with the mass electronic stopping power ratio $[S_{el}/\rho]_{detector}^{water}$ of water to the detectors averaged over the electron fluence in the detector (eq. 3.1). Then the MC dose-to-water D_{water}^{MC} was converted into physical dose-to-water $D_{water}^{Reference}$ under the reference condition with the energy-dependent Monte Carlo reference dose calibration factor N_{MC} (MC dose/1 cGy $\cdot$ MU/primary history) and the number of MU delivered (eq. 3.2). Since the use of N_{MC}

assumed the linac was calibrated in terms of absorbed dose to water to 1 cGy/MU under clinical reference conditions, $D_{water}^{Reference}$ (cGy) was further scaled by the daily output D_{output} (cGy/MU) of the linac to obtain the dose-to-water $D_{water}^{Calibration}$ under the calibration condition(eq. 3.3):

$$D_{water}^{MC} = D_{detector}^{MC} \times [S_{el}/\rho]_{detector}^{water} \tag{3.1}$$

$$D_{water}^{Reference}\,(cGy) = \frac{D_{water}^{MC}}{N_{MC}} \left(\frac{1\ cGy}{MU}\right) \times MU \tag{3.2}$$

$$D_{water}^{Calibration}\,(cGy) = D_{water}^{Reference} \times \frac{D_{output}\,(cGy/MU)}{1\,(cGy/MU)} \tag{3.3}$$

The output D_{output} of the linac was measured using an ion chamber in water at the reference depth d_{ref} under the reference condition described in the AAPM Task Group 51 (TG-51) protocol [7].

3.2.4 Phantom Model Verification

Output Factor Measurement

To ensure the model of the blueprint-defined MapCHECK egsphant accurately represents the real MapCHECK, we validated the egsphant by comparing the simulated and the measured field output factors. MLC-defined 3 cm $\times$ 3 cm, 5 cm $\times$ 5 cm, 8 cm $\times$ 8 cm and 10 cm $\times$ 10 cm fields were delivered to the MapCHECK at 100 cm SSD, and the dose to the centre detector was measured and simulated. The field output factors were defined

as the ratio of the dose to the centre detector in a given field to the dose in the 10 cm $\times$ 10 cm field. The experiment was performed for a 6 MV photon beam and a 12 MeV electron beam.

10 cm x 10 cm Fields Measurement

To validate the MapCHECK performance at each beam energy, 10 cm x 10 cm fields of different energies (6 MV, 6 MeV, 9 MeV, 12 MeV, 16 MeV and 20 MeV) were delivered to the MapCHECK and simulated on the MapCHECK egsphant. The measured and expected dose to each MapCHECK detector was obtained from the measurement data and the MC simulation respectively. The dose distributions of simulation and measurement were compared through a global gamma analysis with a gamma criterion of 3%/2mm and a low dose threshold of 10%.

3.2.5 MBRT Plans Measurement

Treatment Plans and Delivery

In addition to the plan for patient 1, a plan for another STS patient (patient 2) was prepared for MapCHECK measurements. This plan comprises step-and-shoot deliveries of a 6 MV photon beam and electron beams of 5 energies at 100 cm SAD (Table. 3.2). Fig. 3.5 shows a CT slice of the patient with the contour of the CTV. The yellows arrows indicate the delivery angles of the photon beams and the white arrows indicate that of the electron beams. The patient plan was transposed onto the MapCHECK setup on Brems with the isocentre positioned at the centre detector.

Particles	Energy	Angle	SAD (cm)
Photon	6X	(-25°, 9°, 43°, 77°, 111°, 145°, 179°)	100
Electron	6E, 9E, 12E, 16E, 20E	(-10°, 50°, 130°)	100

Table 3.2: Summary of the MBRT plan for patient 2

Since MapCHECK is a two-dimensional dosimetric tool, beams being delivered at larger gantry angle will experience high attenuation when entering the MapCHECK. To validate our MapCHECK model in a simplistic condition, the two plans were delivered to the MapCHECK with collapsed gantry angle at 0 degree. This was to minimize the complications due to attenuation and scattering when beams entering the MapCHECK from the sides or travelling through the couch. This can ensure any discrepancy observed between the measurements and the simulations was due to the MapCHECK model.

Although the plan for patient 2 was optimized at 100 cm SAD, it was delivered at both 80 cm SAD and 100 cm SAD to examine the dependence of the measurement on the distance of delivery. Same as the delivery of patient 1's plan, the plan consists of six .xml plan files and the measurement was made for each energy components separately. Upon completion of the delivery, the individual measurement text files were summed to derive the total distribution of the whole plan.

Dose Comparison

The simulated dose distributions were compared to the measured distributions. The MC dose and the measured dose to each detector voxel were retrieved from the 3ddose file and the measurement text file, respectively. In the delivery of the MBRT plan, the beam quality to the phantom varied voxel by voxel. This was because the energy spectrum of

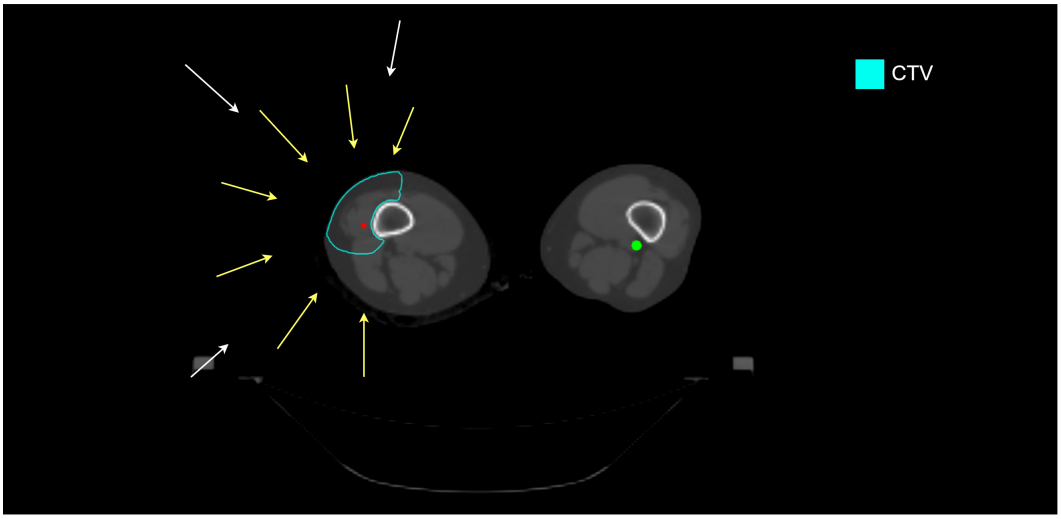

Figure 3.5: A CT slice of patient 2 with the delivery angles indicated.

the beam varies with the scattering condition at different positions. Electron beams experience intensity modulation and scattering when travelling through the MLCs and the phantom. The loss of electron energy could lead to significant changes in the beam energy spectrum. To correct for the difference in beam quality between the calibration condition and the MBRT field, a correction factor for each voxel i in the MapCHECK phantom was derived using the stopping power ratio $[[S_{el}/\rho]^{water}_{detector}]^{MBRT}$ of water to detector at a voxel i in the MapCHECK phantom under the measurement condition, and the stopping power ratio of water to detector at the centre detector of the MapCHECK phantom under the calibration condition [28]:

$$D^{MBRT}_{water,i}\ (cGy) = D^{Calibration}_{water,i} \times \frac{[[S_{el}/\rho]^{water}_{detector}]^{MBRT}_{i}}{[[S_{el}/\rho]^{water}_{detector}]^{Calibration}_{centre}} \tag{3.4}$$

The stopping power ratios for each voxel in the MapCHECK were calculated with the SPRXYZnrc Monte Carlo code, which was modified from the SPRRZnrc and DOSXYZnrc code. By importing the stopping power ratio scoring routine of the SPRRZnrc code into

the DOSXYZnrc code, the stopping power ratio can be scored in the same phantom that was used for DOSXYZnrc dose calculation.

The agreement between the measured and the simulated dose distribution was evaluated using gamma analysis with a gamma criterion of 3%/2mm and a threshold of 10%.

Chapter 4

Results

This chapter presents the experimental results of the study. The first section focuses on the comparisons between the planned and the log file-recalculated dose to the patient's CTV and OARs. The second section reports the results obtained from MapCHECK measurements and Monte Carlo simulations.

4.1 Log file-based Quality Assurance

The MBRT plan for patient 1 was successfully delivered on the three TrueBeam linacs with no interlocks triggered. A total of 12 sets of log file data were collected for dose reconstruction.

4.1.1 Dose Recalculation and Comparison

6×10^7 histories were simulated in the plan dose calculation such that the statistical uncertainties of each energy was below 1 % for voxels receiving more than 50 % of the

maximum dose. The dose distribution in the patient's anatomy from one set of data and the planned dose distribution is shown in Fig. 4.1. Dose profiles were plotted to compare the dose difference between the two dose distributions.

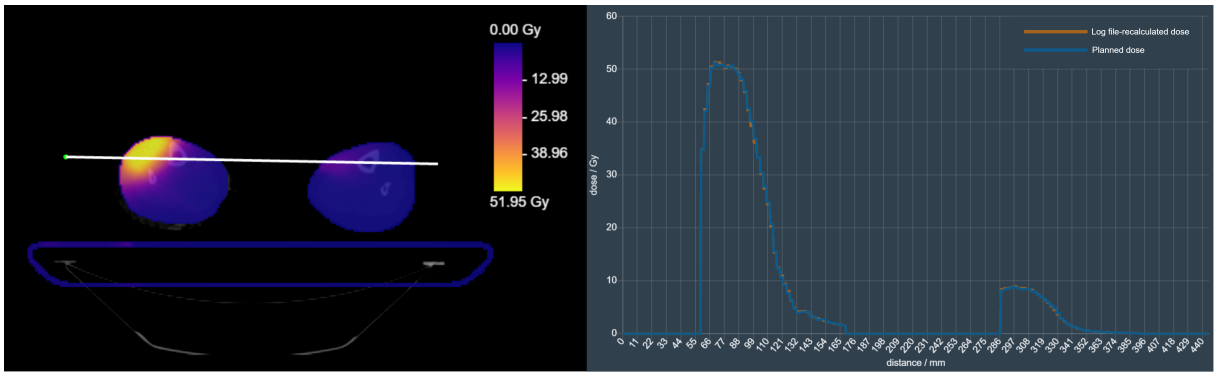

Figure 4.1: The planned and the recalculated dose distribution in the patient's anatomy (left) and their corresponding dose profiles (right).

Inter-linac Difference

To examine the inter-linac difference in the delivery, the recalculated doses to the CTV and OARs across TB3, TB4 and TB5 are shown in Table. 4.1 and Table. 4.2. The deviations between the recalculated and the planned mean dose to the CTV varied between -0.031 % to 0.079 %. For the OARs, which contain more low dose regions that are plagued with higher statistical uncertainty, the dose deviations ranged from -0.02 % to 2.07 %. There was no dependence observed between linacs and the log file dose.

Intra-linac Difference

For intra-linac variation, which expresses the reproducibility of a delivery by a given linac, the mean, minimum and maximum dose over 10 sets of data collected from TB5 are tabulated in Table. 4.3. The recalculated dose to the CTV in 10 deliveries varied from 51.79

Table 4.1: Comparison between the planned and recalculated mean dose to the CTV from 3 deliveries on different linacs.

	CTV		
Theoretical dose (Gy)	51.795		
Log file dose (Gy)	TB3	TB4	TB5
	51.818	51.779	51.836
Difference (%)	0.044	-0.031	0.079

Table 4.2: Comparison between the planned and recalculated mean dose to the OARs from 3 deliveries on different linacs.

	Normal Tissue Ring			Bone (Right leg)			Tissue Strip		
Theoretical dose (Gy)	17.01			1.98			0.482		
Log file dose (Gy)	TB3	TB4	TB5	TB3	TB4	TB5	TB3	TB4	TB5
	17.01	17.01	17.02	1.99	1.99	1.99	0.492	0.491	0.491
Difference (%)	0.01	-0.02	0.04	0.61	0.61	0.61	2.07	1.87	1.87

Gy to 51.84 Gy with a mean of 51.83 Gy. The recalculated mean CTV dose differed from the planned dose by 0.058 %. The differences between the planned and the recalculated dose for the OARs were all below 2.1 %. The log file-recalculated dose exhibited high reproducibility across deliveries and small deviations from the planned dose.

Table 4.3: Comparison between planned and recalculated mean dose from 10 deliveries on TB5 linac.

	CTV		Normal Tissue Ring		Bone (Right leg)		Tissue Strip	
Theoretical dose (Gy)	51.80		17.01		1.978		0.482	
	Min	Max	Min	Max	Min	Max	Min	Max
Log file dose (Gy)	51.79	51.84	17.00	17.02	1.988	1.991	0.490	0.492
	51.83		17.01		1.990		0.491	
	Min	Max	Min	Max	Min	Max	Min	Max
Difference (%)	-0.002	0.093	-0.041	0.035	0.506	0.657	1.660	2.075
	0.058		-0.009		0.581		1.867	

4.2 MapCHECK-based Quality Assurance

4.2.1 Phantom Modelling

A CT MapCHECK egsphant was created from the CT slices of the MapCHECK. The outline of the MapCHECK body and the silicon detectors were automatically contoured on Eclipse based on the range of CT numbers (Fig. 4.2). Due to the CT artifacts near the edges of the MapCHECK, the CT numbers were very high at the two sides of the detector array. Since the detectors' contours were drawn automatically according to a specified CT range, the inconsistent CT number along the detector plane led to inaccurate outline of the detectors' structure and position. Furthermore, detailed information regarding the material and composition of the device could not be obtained from the CT MapCHECK egsphant. Compared to the blueprint-defined MapCHECK egsphant, this model assumed a very simplistic structure for the device and failed to represent the real MapCHECK model.

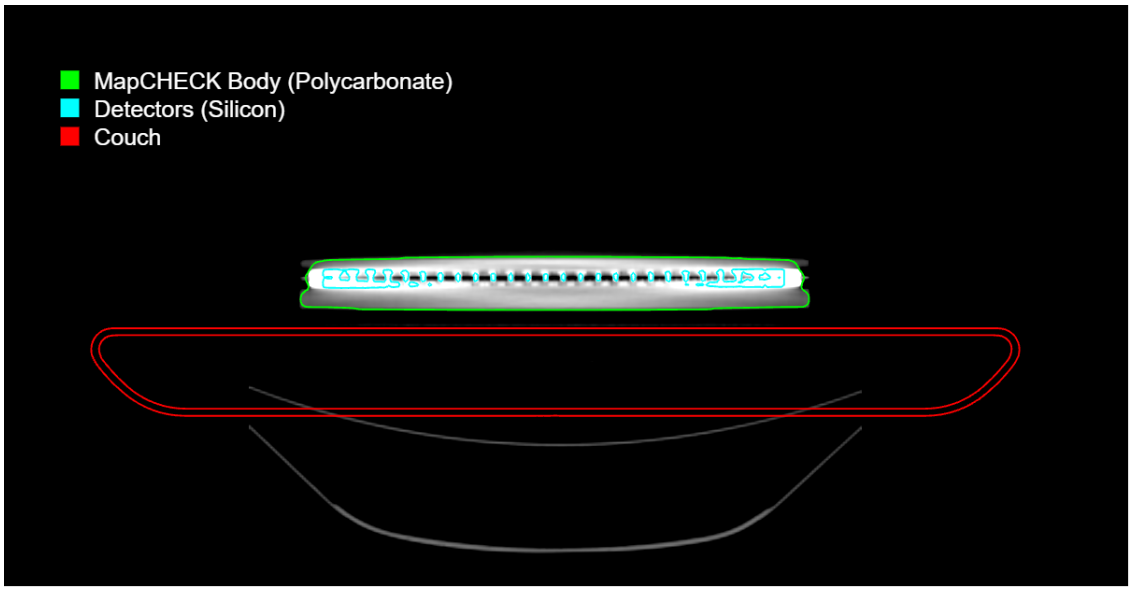

Figure 4.2: The CT slice of the MapCHECK with the contours for the MapCHECK body, silicon detectors and the couch.

A blueprint-defined MapCHECK egsphant was generated. A screenshot of the egsphant on dosxyz_show is shown in Fig. 4.3. The staggered pattern of the detector arrangement and the dimension of each detector were modelled in detail. Compared to the CT MapCHECK egsphant, the blueprint-defined MapCHECK egsphant represented the structure of the device in a more precise and realistic manner. Since the blueprint-defined MapCHECK egsphant was adopted to be the standard Monte Carlo phantom for all the MapCHECK simulations in this study, it will be referred to as "MapCHECK egsphant" in the following texts.

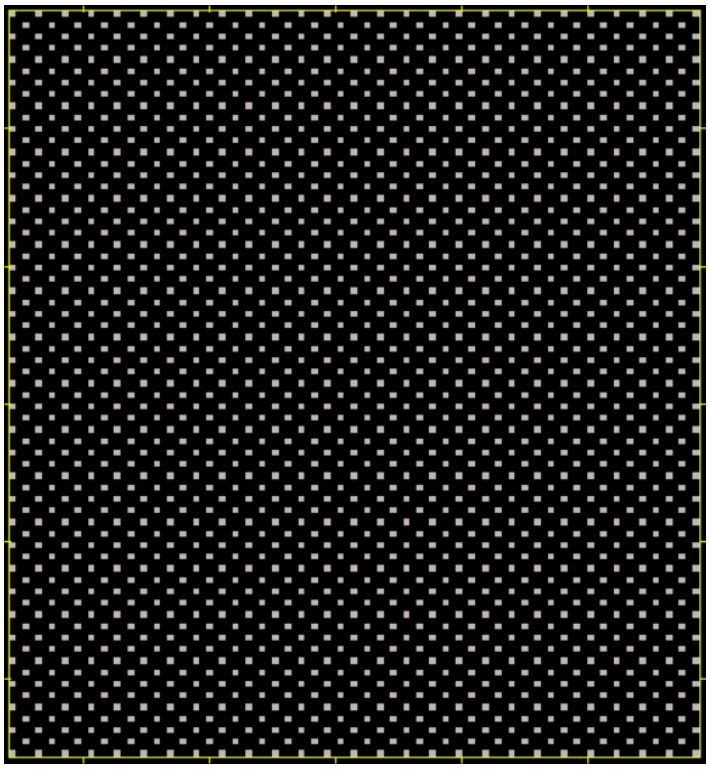

Figure 4.3: A screenshot of the blueprint-defined MapCHECK egsphant on dosxyz_show showing the detector arrangement.

4.2.2 Phantom Model Verification

Output Factor Measurement

To validate the MapCHECK egsphant, the measured and simulated output factors were compared. The measured and simulated dose to the centre detector for each field size were obtained for output factors calculation. The statistical uncertainty of the centre detector dose for all energies and field sizes was less than 0.2 %. The dose to the centre detector and the output factors for 6 MV and 12 MeV radiation fields were shown in Table. 4.4 and Table. 4.5, respectively.

Table 4.4: The comparison between the simulated and measured output factors for a 3 x 3 cm^2, 5 x 5 cm^2, 8 x 8 cm^2 and 10 x 10 cm^2 6 MV field.

6 MV	Simulation		Measurement		% Difference
Field size (cm2)	Detector dose (Gy)	Output factor	Detector dose (Gy)	Output factor	
3 x 3	83.21	0.932	83.66	0.938	-0.646
5 x 5	86.46	0.968	86.62	0.971	-0.296
8 x 8	88.65	0.993	88.77	0.995	-0.239
10 x 10	89.27	1	89.18	1	0

Table 4.5: The comparison between the simulated and measured output factors for a 3 x 3 cm^2, 5 x 5 cm^2, 8 x 8 cm^2 and 10 x 10 cm^2 12 MeV field.

12 MeV	Simulation		Measurement		% Difference
Field size (cm2)	Detector dose (Gy)	Output factor	Detector dose (Gy)	Output factor	
3 x 3	34.23	0.458	33.40	0.444	3.274
5 x 5	58.52	0.783	57.84	0.768	1.934
8 x 8	72.06	0.964	72.29	0.960	0.440
10 x 10	74.75	1	75.31	1	0

The output factor difference for 6 MV fields was within 1 % for all field sizes. For 12 MeV fields, the discrepancies varied from 0.44 % for the 8 cm x 8 cm field to 3.27% for the 3 cm x 3 cm field. The output factor reduced with radiation field size due to the lack of electron lateral scatter equilibrium. The deviations between simulation and measurement

were larger for electron beams and smaller field sizes. This suggests that the MC model may be less accurate at smaller fields.

10 cm x 10 cm Fields Measurement

10 cm by 10 cm fields of different beam energies were delivered to the MapCHECK to examine model's accuracy at each energy. The gamma passing rate for all energies are tabulated in Table. 4.6. The agreement between the simulated and measured dose distribution of all energies has a gamma passing rate of above 95 % except for 6E, which has a passing rate of 88.3 %. The isodose line contour and the gamma map for the 6 MeV and 12 MeV 10 cm x 10 cm field are shown in Fig. 4.4 and Fig. 4.5.

Table 4.6: The gamma passing rate with a gamma criteria of 3%/2mm of the 10 cm x 10 cm field for each energy.

Beam Energy	6X	6E	9E	12E	16E	20E
Gamma passing rate (%)	96.59	88.26	100.00	100.00	99.76	100.00

4.2.3 MBRT Plans Measurement

Patient 1

The MBRT plan for Patient 1 was delivered to the MapCHECK with collapsed gantry angle. The measured and simulated dose distribution were compared (Fig. 4.6). The MU and gamma passing rate for each beam energy in the plan are shown in Table. 4.7. The gamma passing rate for all energy components were above 90 %. The gamma passing rate of the whole plan reached 97.78 %.

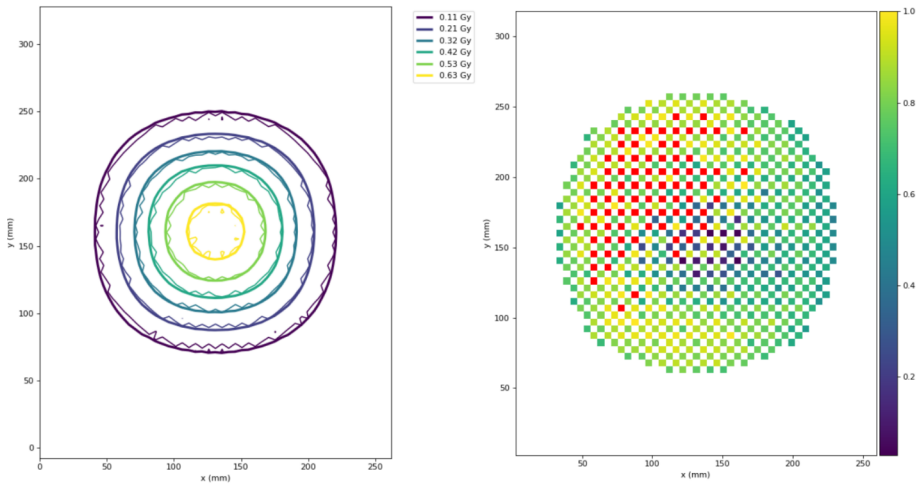

Figure 4.4: The isodose line contour (left) and the gamma map (right) of the 6 MeV 10 cm x 10 cm field. The thin and thick isodose line indicated the measurement and the simulation, respectively.

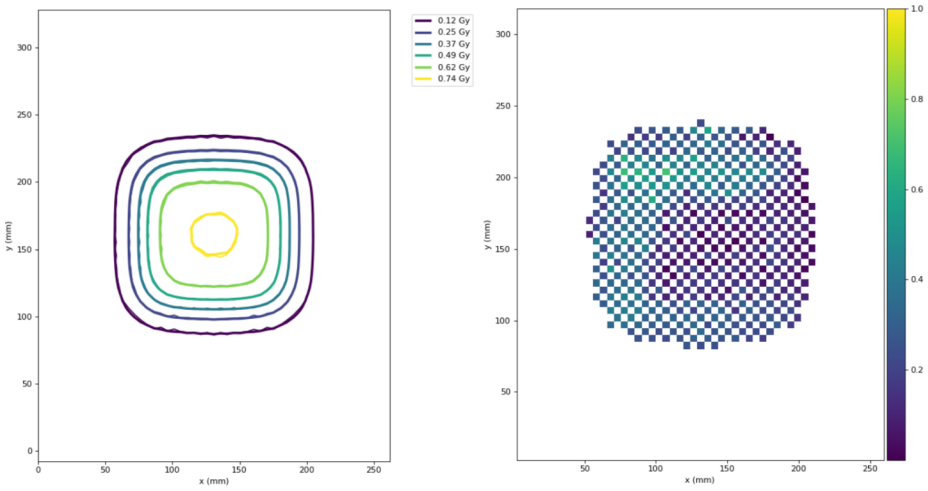

Figure 4.5: The isodose line contour (left) and the gamma map (right) of the 12 MeV 10 cm x 10 cm field.

Patient 2

The MBRT plan for patient 2 was delivered to the MapCHECK with collapsed gantry angle at 80 cm SAD and 100 cm SAD to compare the effect of delivery distance on the agreement of measurements with calculations. Table. 4.8 shows the MU and gamma

Table 4.7: The gamma passing rate with a gamma criteria of 3%/2mm of MBRT plan for patient 1.

Beam Energy	6X	6E	9E	12E	16E	20E	Total
MU	2687.6	3695.2	6786.6	2525.4	401	2085	17179.7
Gamma passing rate (%)	93.86	98.33	98.37	100.00	93.22	90.58	97.78

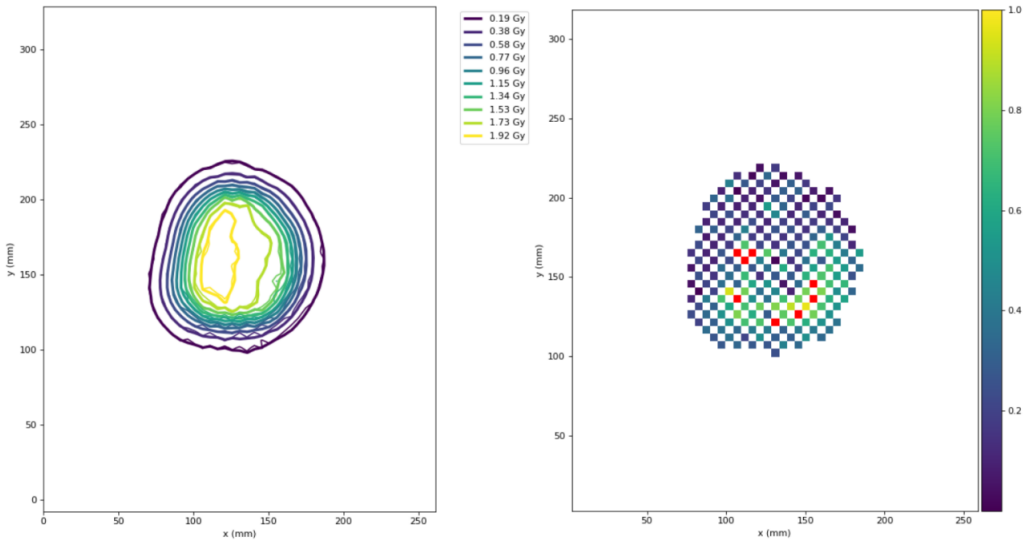

Figure 4.6: The isodose line contour (left) and the gamma map (right) of the MBRT plan dose distribution for patient 1.

passing rate for the plan at two different SADs. The dose distribution and the gamma map for the two deliveries are shown in Fig. 4.7 and Fig. 4.8. The 80 cm SAD delivery showed higher gamma passing rates compared to using 100 cm SAD for all energy components except for 6X. The gamma passing rate for the total plan reached 97.1 % using an 80 cm SAD, while it was 84.55 % when delivered at 100 cm SAD.

Table 4.8: The gamma passing rate with a gamma criteria of 3%/2mm for the MBRT plan for patient 2.

Beam Energy	6X	6E	9E	12E	16E	20E	Total
MU	5764.1	6336.4	8478.4	11707.1	5346.3	7126.3	44758.6
Gamma passing rate (%) (80 cm SAD)	92.62	98.35	98.61	99.34	98.45	96.13	97.10
Gamma passing rate (%) (100 cm SAD)	94.53	74.50	85.46	94.91	91.73	81.76	84.55

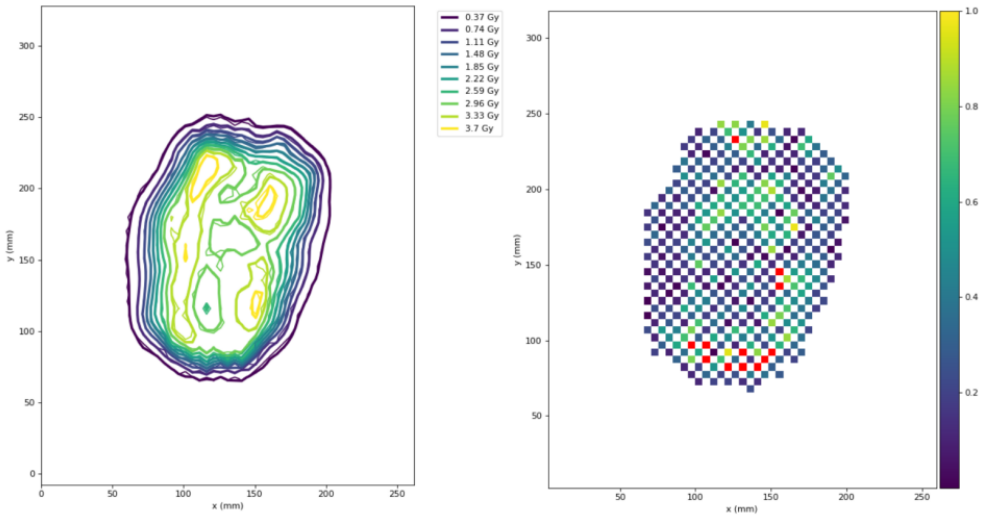

Figure 4.7: The isodose line contour (left) and the gamma map (right) of the MBRT plan dose distribution for patient 2 delivered at 80 cm SAD.

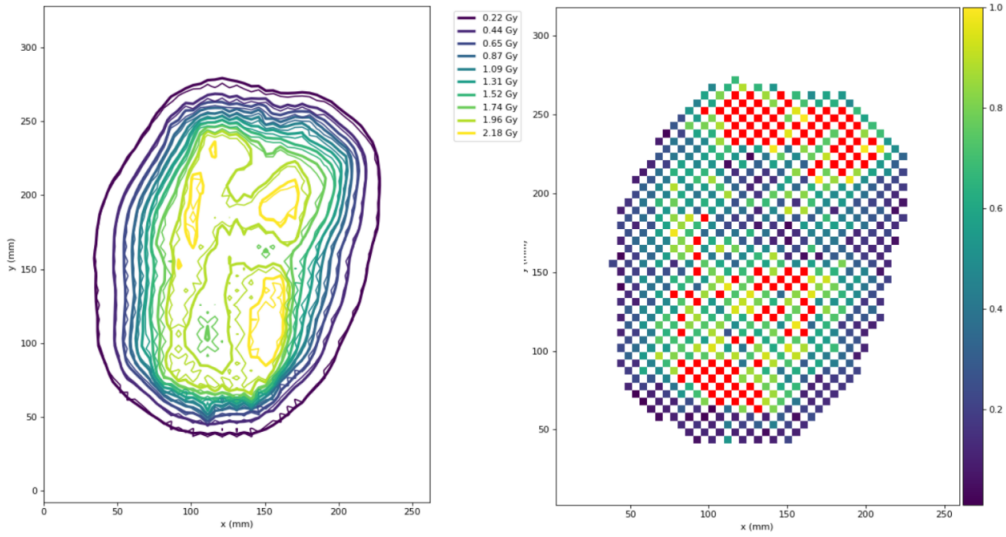

Figure 4.8: The isodose line contour (left) and the gamma map (right) of the MBRT plan dose distribution for patient 2 delivered at 100 cm SAD.

Chapter 5

Discussions

This chapter discusses the measurement results and provides possible explanations for the deviations between the expected and the actual outcomes. We will also compare our work with previous studies and deliberate our future directions in this project.

5.1 Log file-based Quality Assurance

5.1.1 Dose reconstruction using log files

From the results presented, dose distribution reconstructed using log files data showed excellent agreement with the planned dose distribution with no inter- and intra- linac differences observed. However, in this study, only three Varian TrueBeams and one MBRT plan have been tested. The results may not be generalizable to other machines and MBRT plans.

Previous studies have evaluated the performance of reconstructing VMAT dose distribution in patients' anatomy with log file data [21, 33, 56]. Qian *et al*. (2010) updated the DICOM-RT file with log file data after delivery and reconstructed the delivered dose distribution on the CBCT-based patient model with the anisotropic analytical algorithm (AAA) on Eclipse [56]. Defoor *et al*. (2015) and Katsuta *et al*. (2017) adopted similar methods to reconstruct VMAT dose distribution using Pinnacle TPS and Monaco TPS respectively [21, 33]. All studies demonstrated the agreement between the planned and reconstructed dose distribution for VMAT plans. In addition to photon beams in VMAT, MBRT plans involve also electron beams. In this study, we extended the use of log file-dose reconstruction to electron deliveries and demonstrated the feasibility of recalculating dose distributions with log file data for both photon and electron beams.

An advantage of using log file-dose reconstruction for QA is that the planned dose and the recalculated dose are obtained using the same algorithm [21]. This eliminates any difference in the quality and accuracy of the two dose distributions and enables a fair comparison. Any deviations observed between the planned and the recalculated dose can be attributed to machine performance and the delivery errors can be easily pinpointed. However, the accuracy of the reconstructed dose also relies heavily on the calculation algorithm. In our study, we made sure the number of histories in the MC calculation was large enough such that the uncertainties were below 1 % for all voxels with more than 50 % of the maximum dose. A balance between the computational time and the statistical uncertainty should also be carefully considered.

5.1.2 Error detection sensitivity of Log file-dose reconstruction

In future work, we aim to evaluate the sensitivity of log file-based QA in detecting delivery errors. A commonly used approach to investigate the sensitivity of a QA tool is to generate intended errors manually from the original plan, and examine the ability of the QA method to identify these errors [12, 27, 44]. Heilemann *et al*. (2013) studied the sensitivity of Octavius 2D-Array (PTW-Freiburg) and the Delta4 device (Scandidos) to MLC misalignments by purposely creating MLC displacements of different magnitudes from the original plan [27]. Bedford *et al*. (2014) investigated the performance of using portal imaging to detect VMAT synchronization errors by simulating errors in gantry angle, MU and MLC leaf positions [12]. Liang *et al*. (2016) studied the machine error sensitivity of ArcCHECK, Delta4 and an EPID-based technique by simulating potential delivery errors due to the gravitational effect [44]. These studies were mainly conducted using VMAT plans but their methodology could apply to MBRT plans.

Errors that might occur during MBRT delivery include:

- Gantry angle - MLC desynchronization
- Gantry angle - MU desynchronization
- MLC encoder drift
- Sluggish leaf
- Carriage backlash
- Gravitational shift

To examine the performance of log file-based QA to detect MBRT delivery errors, we can modify the original plan to create multiple erroneous plans that incorporated different types of errors. Errors due to MLC encoder drift and sluggish leaves can be simulated by introducing small shifts in the position of a few MLC leaves. Errors triggered by the gravitational effect can be reproduced by moving all MLC leaves in the same direction by the same magnitude as a function of gantry angle. Creating mismatches between gantry angles and MLC apertures can also mimic desynchronization. After delivering the erroneous plans, we can again collect log files for dose calculation and compare the reconstructed dose with the original planned dose. To study the sensitivity of log file-reconstruction, we should introduce errors of various magnitudes to see what is the minimum error to cause a ”noticeable difference” between the two dose distributions.

5.2 MapCHECK-based Quality Assurance

5.2.1 MapCHECK Calibration

Array Calibration

In the array calibration, the MapCHECK was calibrated with a 6 MV photon field and a 12 MeV electron field. Separated calibration files were used to apply correction factors to photon and electron measurement to account for the potential energy dependence of the detectors. Ideally, array calibration could be conducted for each energy in the MBRT plan to further eliminate the effect of energy dependence. We have tested using a 12 MeV and a 16 MeV array calibration file to correct a 16 MeV measurement and the results show

minimal differences. Therefore, we decided to use the 12 MeV array calibration for all electron energies as 12 MeV is in the middle of the range of electron energies in the MBRT plans.

A minor problem we observed during the array calibration was that the 37 cm x 37 cm 6 MV field measured by the MapCHECK showed a slightly asymmetric beam profile along the x-axis (Fig. 5.1). This could possibly be due to the asymmetric beam delivered by the linac or the incorrect levelling of the MapCHECK. This could affect the quality of the calibration because a flat and symmetric profile is required to measure the relative sensitivity differences between the detectors. An asymmetric profile may lead to incorrect calculation of the correction factors for each detector. However, based on the measurement results of the 10 cm x 10 cm fields (Table. 4.6), the asymmetry did not have a significant effect on the gamma passing rates with the criteria of 3%/2mm.

Absolute dose Calibration

In the absolute dose calibration, the MapCHECK was calibrated to the known absolute dose-to-water $D_{water}^{Calibration}$ at the detector depth under reference condition. At preliminary stages of the study, we attempted to derive $D_{water}^{Calibration}$ by simply scaling down the reference dose using a PDD table. The dose to the centre detector was thus calculated as the dose in reference conditions, at $d_{\max}$, multiplied by the PDD at 2 cm water-equivalent depth for each energy. However, the results for the MBRT plans measurement showed poor agreement with the planned dose distributions. We suspected that the 2 cm water-equivalent thickness of polycarbonate advertised by the manufacturer may not be applicable to all beam energies. Therefore, we decided to model a MapCHECK phantom

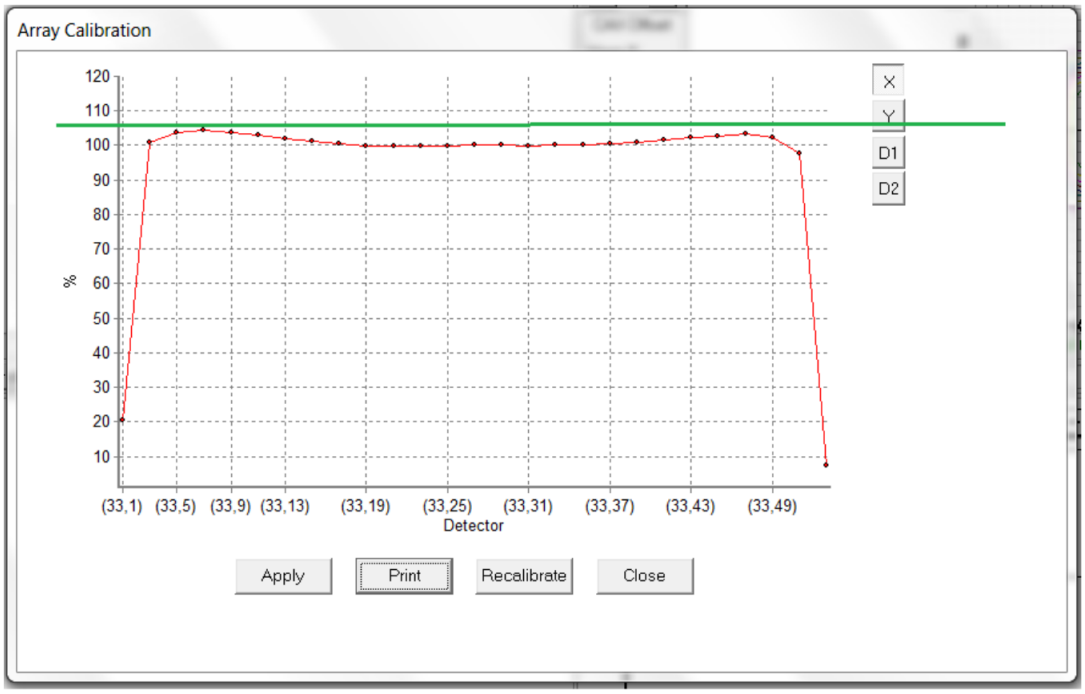

Figure 5.1: The measured beam profile of a 37 cm x 37 cm 6 MV field along the x-axis. A green horizontal line was drawn for determining the beam symmetry.

on EGSnrc and calculate the corresponding $D_{water}^{Calibration}$ for each energy with Monte Carlo simulation. The results of output factor measurement (Table. 4.4 & Table. 4.5) and 10 cm x 10 cm fields measurement (Table. 4.6) validated the model and the absolute dose calibration of the MapCHECK. With the verified MapCHECK MC phantom and an accurately calibrated MapCHECK device, we could proceed to MBRT plans measurement.

5.2.2 Effect of Delivery distance on Measurement Results

The agreement between the measured and planned dose distribution for the two MBRT plans was presented in Table. 4.7 and Table. 4.8. The results for the patient 1's plan, in which the electron beams were delivered at an 80 cm SAD, and the 80 cm SAD delivery of patient 2's plan showed excellent gamma passing rate in the total delivery and the

passing rate for all energy components were above 90 %. For the 100 cm SAD delivery of patient 2's plan, the gamma passing rate for all energy components were lower than the 80 cm SAD delivery except for 6X. The results showed a strong dependence of the gamma passing rate for electron energies on the delivery distance. A possible cause could be that the scattering effect of electron beams were not accurately modelled in the simulations. When the beam was delivered at 80 cm SAD, the particles went through a shorter distance in the air and experience less scattering. Therefore, the potentially inaccurate model has less effect on the deliveries with a shortened SAD. The gamma passing rate for 6E was the worst among all electron energies in the 100 cm SAD delivery of the plan as well as the 10 cm x 10 cm field delivery, which had an SSD of 100 cm. Due to the steep dose gradient of the depth dose curve, the low energy electron beams are more sensitive to any inaccuracies in the detector model and the beam model. Although the MapCHECK MC phantom was modelled according to the specifications described by the blueprint, there might be some manufacturing uncertainties. Small errors in the detector dimensions including effective detector volume and effective depth can be accentuated and lead to considerable dose differences between measurement and simulation. Inaccuracies in the Monte Carlo beam model could also lead to discrepancies with measurements. Although we used Varian-supplied phase space files as our beam source, these phase space files are generated for a generic TrueBeam linac, and may have very slightly different energy spectrum from our clinical ones. The phase spaces are also positioned upstream from the jaws and MLCs. Inaccuracies in our MLC models could have larger impact at lower electron energies.

To conclude, the measured and simulated dose distributions showed excellent agreement in both plans when an 80 cm SAD was used for electron deliveries. Although the agreement was lower in one or more energy components, the discrepancies had only a minor impact on the performance of the combined delivery. In this study, only two MBRT plans were tested. The lower passing rate for a certain energy component could be due to a specific aperture but not the beam energy. In the future, we will continue investigating more MBRT plans and try to pinpoint the problem.

5.2.3 Non-collapsed Delivery

Ideally, the MapCHECK measurement and collection of treatment log files can be performed in a single delivery with varying gantry angles to provide both a measurement-based and calculation-based QA for an MBRT plan at the same time. However, being a two-dimensional detector array, the capability of MapCHECK in measuring radiation from large gantry angles remains to be tested.

The major issue of using MapCHECK to measure dose from non-collapsed delivery was that the beam delivered at large gantry angles will experience high attenuation in the MapCHECK phantom and the couch before reaching the detectors (Fig. 5.2). For the simulation of a non-collapsed delivery, not only the detector array but the case of the MapCHECK should also be carefully modelled. To validate the model for non-collapsed delivery, delivery of simple fields at different gantry angles will need to be made to ensure that the model can correctly simulate the beam entering from all angles.

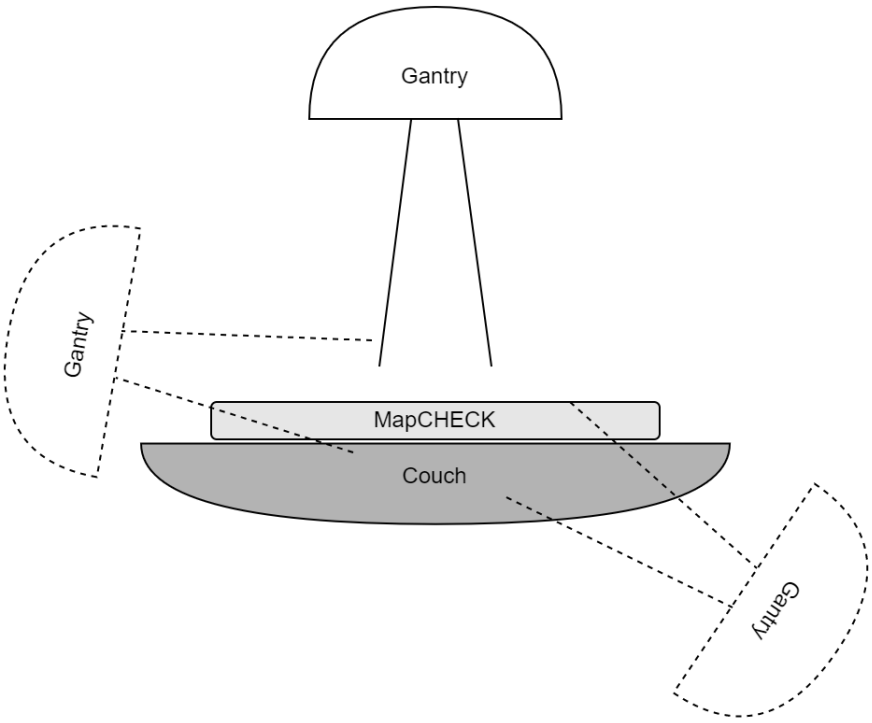

Figure 5.2: The beam from large gantry angles experience high attenuation in the MapCHECK phantom and the couch.

Chapter 6

Conclusion

In this study, we examined the feasibility of using log files and MapCHECK for MBRT plan verification. Two MBRT plans for two soft tissue sarcoma patients were optimized for the study. The MBRT plans consist of a 6 MV photon beam, and electron beams of 6 MeV, 9 MeV, 12 MeV, 16 MeV and 20 MeV.

To evaluate the performance of log file-based QA for MBRT, an MBRT plan was delivered on three Varian TrueBeams and treatment log files were collected for dose reconstruction in the patient anatomy using the EGSnrc Monte Carlo system. The planned and the recalculated dose to the PTV and three OARs were compared with intra-linac and inter-linac differences taken into consideration. The deviations in the dose to PTV were below 0.1 % in all deliveries across three different linacs. The difference in the dose to the three OARs varied between -0.02 % to 2.07 %. The log file-reconstructed dose showed excellent agreement with the planned dose with no intra- or inter-linac differences observed.

To compare the planned dose and measured dose on the MapCHECK, a MapCHECK Monte Carlo phantom was modelled on EGSnrc for dose simulation. The phantom was

validated through field output factors measurement and 10 cm x 10 cm fields measurement. Two MBRT plans were delivered to the MaPCHECK with collapsed gantry angle at 0° and the agreement between the measurement and simulation was evaluated using gamma analysis with gamma criteria of 3%/2mm. The gamma passing rate for the total delivery reached 97 % for both plans when the electron beams were delivered at an 80 cm SAD. The gamma passing rate dropped to 85 % when the SAD was increased to 100 cm SAD. For individual energy components, 6E showed the strongest dependence on delivery distance, possibly due to the significant scattering effect of low energy electrons.

This study demonstrated the potential of log files and MapCHECK as MBRT QA tools. The next step in this study will be to examine the capability of MapCHECK to measure non-collapsed delivery. The sensitivity of the two methods will also be studied by creating errors artificially in the delivery.

Bibliography

[1] ABDEL-RAHMAN, W., AND PODGORSAK, E. Energy transfer and energy absorption in photon interactions with matter revisited: A step-by-step illustrated approach. *Radiation Physics and Chemistry - RADIAT PHYS CHEM 79* (05 2010), 552–566.

[2] AGOSTINELLI, S. Geant4—a simulation toolkit. *Nuclear Instruments and Methods in Physics Research Section A: Accelerators, Spectrometers, Detectors and Associated Equipment 506*, 3 (2003), 250–303.

[3] AL-YAHYA, K., SCHWARTZ, M., SHENOUDA, G., VERHAEGEN, F., FREEMAN, C., AND SEUNTJENS, J. Energy modulated electron therapy using a few leaf electron collimator in combination with imrt and 3d-crt: Monte carlo-based planning and dosimetric evaluation. *Medical Physics 32*, 9 (2005), 2976–2986.

[4] AL-YAHYA, K., VERHAEGEN, F., AND SEUNTJENS, J. Design and dosimetry of a few leaf electron collimator for energy modulated electron therapy. *Medical Physics 34*, 12 (2007), 4782–4791.

[5] ALDER, B. *Methods in Computational Physics*. No. v. 1 in Methods in Computational Physics. Academic Press, 1963.

[6] ALEXANDER, A., SOISSON, E. T., RENAUD, M., AND SEUNTJENS, J. Direct aperture optimization for flec-based mert and its application in mixed beam radiotherapy. *Medical physics 39 8* (2012), 4820–31.

[7] ALMOND, P. R., BIGGS, P. J., COURSEY, B. M., HANSON, W. F., HUQ, M. S., NATH, R., AND ROGERS, D. W. O. Aapm's tg-51 protocol for clinical reference dosimetry of high-energy photon and electron beams. *Medical Physics 26*, 9 (1999), 1847–1870.

[8] ARISTOPHANOUS, M., SUH, Y., CHI, P., WHITTLESEY, L., LANEAVE, S., AND MARTEL, M. Initial clinical experience with arccheck for imrt/vmat qa. *Journal of applied clinical medical physics 17* (09 2016), 6118.

[9] BARÓ, J., SEMPAU, J., FERNÁNDEZ-VAREA, J., AND SALVAT, F. Penelope: An algorithm for monte carlo simulation of the penetration and energy loss of electrons and positrons in matter. *Nuclear Instruments and Methods in Physics Research Section B: Beam Interactions with Materials and Atoms 100*, 1 (1995), 31–46.

[10] BASKAR, R., LEE, K. A., YEO, R., AND YEOH, K.-W. Cancer and radiation therapy: Current advances and future directions. *International Journal of Medical Sciences 9*, 3 (2012), 193–199.

[11] BAWAZEER, O. *EPID based transit dosimetry to monitor inter-fraction variation in radiation therapy*. PhD thesis, RMIT University, 2018.

[12] BEDFORD, J., CHAJECKA-SZCZYGIELSKA, H., AND THOMAS, M. Quality control of vmat synchronization using portal imaging. *Journal of applied clinical medical physics / American College of Medical Physics 16* (02 2015), 5238.

[13] BERGER, M. J., COURSEY, J. S., ZUCKER, M. A., AND CHANG, J. Stopping power and range tables for electrons in water.

[14] BETHE, H., HEITLER, W., AND DIRAC, P. A. M. On the stopping of fast particles and on the creation of positive electrons. *Proceedings of the Royal Society of London. Series A, Containing Papers of a Mathematical and Physical Character 146*, 856 (1934), 83–112.

[15] BLOMQUIST, M., KARLSSON, M., ZACKRISSON, B., AND KARLSSON, M. Multileaf collimation of electrons - clinical effects on electron energy modulation and mixed beam therapy depending on treatment head design. *Physics in medicine and biology 47* (05 2002), 1013–24.

[16] BORTFELD, T. Imrt: a review and preview. *Physics in Medicine and Biology 51*, 13 (2006).

[17] BOYER, A. L., BIGGS, P. J., GALVIN, J. M., KLEIN, E. E., LOSASSO, T. J., LOW, D. A., MAH, K., AND YU, C. X. *Basic Applications of Multileaf Collimators*. AAPM report. American Association of Physicists in Medicine, 2001.

[18] CHETTY, I. J., CURRAN, B., CYGLER, J. E., DEMARCO, J. J., EZZELL, G., FADDEGON, B. A., KAWRAKOW, I., KEALL, P. J., LIU, H., MA, C.-M. C., ROGERS, D. W. O., SEUNTJENS, J., SHEIKH-BAGHERI, D., AND SIEBERS, J. V. Report of the aapm task group no. 105: Issues associated with clinical implementation of monte carlo-based photon and electron external beam treatment planning. *Medical Physics 34*, 12 (2007), 4818–4853.

[19] CHIN, M. History-by-history variance in monte carlo simulation of radiation interactions with matter. *Applied Mathematics 08* (01 2017), 293–306.

[20] CHUANG, K.-C., GILES, W., AND ADAMSON, J. On the use of trajectory log files for machine & patient specific qa. *Biomedical Physics & Engineering Express 7*, 1 (2020), 015010.

[21] DEFOOR, D. L., VAZQUEZ-QUINO, L. A., MAVROIDIS, P., PAPANIKOLAOU, N., AND STATHAKIS, S. Anatomy-based, patient-specific vmat qa using epid or mlc log files. *Journal of Applied Clinical Medical Physics 16*, 3 (2015), 206–215.

[22] DONG, L., ANTOLAK, J., SALEHPOUR, M., FORSTER, K., O'NEILL, L., KENDALL, R., AND ROSEN, I. Patient-specific point dose measurement for imrt monitor unit verification. *International journal of radiation oncology, biology, physics 56* (08 2003), 867–77.

[23] DYK, J. V. *The modern technology of radiation oncology. a compendium for medical physicists and radiation oncologists*. Medical Physics Pub., 2020.

[24] EZZELL, G. A., BURMEISTER, J. W., DOGAN, N., LOSASSO, T. J., MECHALAKOS, J. G., MIHAILIDIS, D., MOLINEU, A., PALTA, J. R., RAMSEY, C. R., SALTER, B. J., SHI, J., XIA, P., YUE, N. J., AND XIAO, Y. Imrt commissioning: Multiple institution planning and dosimetry comparisons, a report from aapm task group 119. *Medical Physics 36*, 11 (2009), 5359–5373.

[25] FENOGLIETTO, P., LALIBERTÉ, B., AILLERES, N., RIOU, O., DUBOIS, J.-B., AND AZRIA, D. Eight years of imrt quality assurance with ionization chambers and film

dosimetry: experience of the montpellier comprehensive cancer center. *Radiation oncology (London, England) 6* (07 2011), 85.

[26] GRUBBÉ, E. H. Priority in the therapeutic use of x-rays. *Radiology 21*, 2 (1933), 156–162.

[27] HEILEMANN, G., POPPE, B., AND LAUB, W. On the sensitivity of common gamma-index evaluation methods to mlc misalignments in rapidarc quality assurance. *Medical physics 40* (03 2013), 031702.

[28] HENG, V. J., SERBAN, M., SEUNTJENS, J., AND RENAUD, M.-A. Ion chamber and film-based quality assurance of mixed electron-photon radiation therapy. *Medical Physics 48*, 9 (2021), 5382–5395.

[29] HOLSTI, L. R. Development of clinical radiotherapy since 1896. *Acta Oncologica 34*, 8 (1995), 995–1003.

[30] JANSSON, T., LINDMAN, H., NYGÅRD, K., DAHLGREN, C. V., MONTELIUS, A., ÖBERG KREUGER, C., ASPLUND, S., AND BERGH, J. Radiotherapy of breast cancer after breast-conserving surgery: an improved technique using mixed electron–photon beams with a multileaf collimator. *Radiotherapy and Oncology 46*, 1 (1998), 83–89.

[31] JONES, D. Icru report 50—prescribing, recording and reporting photon beam therapy. *Medical Physics 21*, 6 (1994), 833–834.

[32] KARLSSON, M. G., KARLSSON, M., AND MA, C.-M. Treatment head design for multileaf collimated high-energy electrons. *Medical Physics 26*, 10 (1999), 2161–2167.

[33] KATSUTA, Y., KADOYA, N., FUJITA, Y., SHIMIZU, E., MATSUNAGA, K., SAWADA, K., MATSUSHITA, H., MAJIMA, K., AND JINGU, K. Patient-specific quality assurance using monte carlo dose calculation and elekta log files for prostate volumetric-modulated arc therapy. *Technology in Cancer Research & Treatment 16* (2017), 1220 – 1225.

[34] KAWRAKOW, I. Accurate condensed history monte carlo simulation of electron transport. i. egsnrc, the new egs4 version. *Medical physics 27* (04 2000), 485–98.

[35] KAWRAKOW, I., MAINEGRA-HING, E., AND TESSIER, F. The egsnrc code system: Monte carlo simulation of electron and photon transport. *NRCC Report PIRS-701* (04 2021).

[36] KERNS, J. Pylinac. `https://github.com/jrkerns/pylinac`, 2021.

[37] KOREVAAR, E. W., VAN VLIET, R. J., WOUDSTRA, E., HEIJMEN, B. J., AND HUIZENGA, H. Sharpening the penumbra of high energy electron beams with low weight narrow photon beams. *Radiotherapy and Oncology 48*, 2 (1998), 213–220.

[38] KUI MU, X., OLOFSSON, L., KARLSSON, M., SJÖGREN, R., AND ZACKRISSON, B. Can photon imrt be improved by combination with mixed electron and photon techniques? *Acta Oncologica 43* (2004), 727 – 735.

[39] LAMANNA, E., GALLO, A., RUSSO, F., BRANCACCIO, R., SORIANI, A., AND STRIGARI, L. *Modern Practices in Radiation Therapy*. IntechOpen, Rijeka, 03 2012, ch. 9, p. 146.

[40] LEDERMAN, M. The early history of radiotherapy: 1895–1939. *International Journal of Radiation Oncology*Biology*Physics 7*, 5 (1981), 639–648.

[41] LEYBOVICH, L., SETHI, A., AND DOGAN, N. Comparison of ionization chambers of various volumes for imrt absolute dose verification. *Medical physics 30* (02 2003), 119–23.

[42] LI, G., JIE ZHANG, Y., JIANG, X., BAI, S., PENG, G., WU, K., AND JIANG, Q. Evaluation of the arccheck qa system for imrt and vmat verification. *Physica medica : PM : an international journal devoted to the applications of physics to medicine and biology : official journal of the Italian Association of Biomedical Physics 29 3* (2013), 295–303.

[43] LI, H., DONG, L., ZHANG, L., YANG, J. N., GILLIN, M. T., AND ZHU, X. R. Toward a better understanding of the gamma index: Investigation of parameters with a surface-based distance methoda). *Medical Physics 38*, 12 (2011), 6730–6741.

[44] LIANG, B., BO, L., ZHOU, F., YIN, F.-F., AND WU, Q. Comparisons of volumetric modulated arc therapy (vmat) quality assurance (qa) systems: Sensitivity analysis to machine errors. *Radiation Oncology (London, England) 11* (11 2016).

[45] MA, C.-M., PAWLICKI, T., LEE, M. C., JIANG, S. B., LI, J. S., DENG, J., YI, B., MOK, E., AND BOYER, A. L. Energy- and intensity-modulated electron beams for radiotherapy. *Physics in Medicine and Biology 45*, 8 (2000), 2293–2311.

[46] MASSILLON-JL, G., CHIU-TSAO, S.-T., MUÑOZ, I., AND CHAN, M. Energy dependence of the new gafchromic ebt3 film: Dose response curves for 50 kv, 6 and 15 mv

x-ray beams. *International Journal of Medical Physics, Clinical Engineering and Radiation Oncology 1* (08 2012), 60–65.

[47] MIFTEN, M., OLCH, A., MIHAILIDIS, D., MORAN, J., PAWLICKI, T., MOLINEU, A., LI, H., WIJESOORIYA, K., SHI, J., XIA, P., AND ET AL. Tolerance limits and methodologies for imrt measurement-based verification qa: Recommendations of aapm task group no. 218. *Medical Physics 45*, 4 (2018).

[48] MIRAS, H., JIMÉNEZ, R., PERALES, A., TERRÓN, J., BERTOLET, A., ORTIZ, A., AND MACÍAS, J. Monte carlo verification of radiotherapy treatments with cloudmc. *Radiation Oncology 13* (06 2018).

[49] MUELLER, S., FIX, M. K., JOOSTEN, A., HENZEN, D., FREI, D., VOLKEN, W., KUENG, R., AEBERSOLD, D. M., STAMPANONI, M., AND MANSER, P. Simultaneous optimization of photons and electrons for mixed beam radiotherapy. *Physics in medicine and biology 62 14* (2017), 5840–5860.

[50] NAKADA, R., AL-OLA, O. M. A., AND YOSHINAGA, T. Intensity-modulated radiation therapy optimization for acceptable and remaining-one unacceptable dose-volume and mean-dose constraint planning. *Computational and Mathematical Methods in Medicine 2020* (2020), 1–14.

[51] NEILSON, C., KLEIN, M., BARNETT, R., AND YARTSEV, S. Delivery quality assurance with arccheck. *Medical dosimetry : official journal of the American Association of Medical Dosimetrists 38* (08 2012).

[52] NIROOMAND-RAD, A., CHIU-TSAO, S.-T., GRAMS, M. P., LEWIS, D. F., SOARES, C. G., VAN BATTUM, L. J., DAS, I. J., TRICHTER, S., KISSICK, M. W., MASSILLON-JL, G., ALVAREZ, P. E., AND CHAN, M. F. Report of aapm task group 235 radiochromic film dosimetry: An update to tg-55. *Medical Physics 47*, 12 (2020), 5986–6025.

[53] PAI, S., DAS, I. J., DEMPSEY, J. F., LAM, K. L., LOSASSO, T. J., OLCH, A. J., PALTA, J. R., REINSTEIN, L. E., RITT, D., AND WILCOX, E. E. Tg-69: Radiographic film for megavoltage beam dosimetry. *Medical Physics 34*, 6Part1 (2007), 2228–2258.

[54] PODGORSAK, E. B. *Radiation oncology physics: a handbook for teachers and students*. International Atomic Energy Agency, 2005.

[55] PODGORSAK, E. B. *Radiation physics for medical physicists*. Springer, 2016.

[56] QIAN, J., LEE, L., LIU, W., CHU, K., MOK, E., LUXTON, G., LE, Q.-T., AND XING, L. Dose reconstruction for volumetric modulated arc therapy (vmat) using cone-beam ct and dynamic log files. *Physics in medicine and biology 55* (07 2010), 3597–610.

[57] RENAUD, M.-A., SERBAN, M., AND SEUNTJENS, J. On mixed electron–photon radiation therapy optimization using the column generation approach. *Medical Physics 44*, 8 (2017), 4287–4298.

[58] SUCHOWERSKA, N., HOBAN, P., BUTSON, M., DAVISON, A., AND METCALFE, P. Directional dependence in film dosimetry: Radiographic and radiochromic film. *Phys. Med. Biol 46* (05 2001), 1391–1397.

[59] SUN NUCLEAR CORPORATION. *Reference Guide, MapCHECK 2™*. Melbourne, Florida, USA, 2010.

[60] SVEISTRUP, J., ROSENSCHÖLD, P. M. A., DEASY, J. O., OH, J. H., POMMER, T., PETERSEN, P. M., AND ENGELHOLM, S. A. Improvement in toxicity in high risk prostate cancer patients treated with image-guided intensity-modulated radiotherapy compared to 3d conformal radiotherapy without daily image guidance. *Radiation Oncology 9*, 1 (2014).

[61] SYKES, J. R., JAMES, H. V., AND WILLIAMS, P. C. How much does film sensitivity increase at depth for larger field sizes? *Medical Physics 26*, 2 (1999), 329–330.

[62] TAYLOR, A. Intensity-modulated radiotherapy - what is it? *Cancer Imaging 4*, 2 (2004), 68–73.

[63] TEMPLETON, A., CHU, J. C. H., AND TURIAN, J. V. The sensitivity of arccheck-based gamma analysis to manufactured errors in helical tomotherapy radiation delivery. *Journal of Applied Clinical Medical Physics 16* (2015), 32 – 39.

[64] TEOH, M., CLARK, C. H., WOOD, K., WHITAKER, S., AND NISBET, A. Volumetric modulated arc therapy: a review of current literature and clinical use in practice. *The British Journal of Radiology 84*, 1007 (2011), 967–996.

[65] THWAITES, D., AND TUOHY, J. Back to the future: The history and development of the clinical linear accelerator. *Physics in medicine and biology 51* (08 2006), R343–62.

[66] VAN ELMPT, W., MCDERMOTT, L., NIJSTEN, S., WENDLING, M., LAMBIN, P., AND MIJNHEER, B. A literature review of electronic portal imaging for radiotherapy dosimetry. *Radiotherapy and Oncology 88*, 3 (2008), 289–309.

[67] VARIAN MEDICAL SYSTEM. *TrueBeam™ Trajectory Log File Specification*. Palo Alto, California, USA, 2011.

[68] YEO, I., AND KIM, J. *A Procedural Guide to Film Dosimetry with Emphasis on IMRT*. Medical Physics Publishing Corporation, 2004.